Avoidance of tearing modes wall-locking in a reversed field pinch with active feedback coils

To cite this article: P Zanca 2009 *Plasma Phys. Control. Fusion* **51** 015006

View the article online for updates and enhancements.

Avoidance of tearing modes wall-locking in a reversed field pinch with active feedback coils

P Zanca

Consorzio RFX, Associazione Euratom_ENEA sulla Fusione, Padova, Italy

Abstract

A general analysis of the feedback on the dynamo tearing modes (TMs) in a cylindrical force-free reversed field pinch equipped with an active coils grid is shown. A single resistive shell with thickness much smaller than its minor radius is considered. Nevertheless, the radial field variation across the shell is taken into account. The active coils are placed outside the shell. The model describes the evolution of several TMs at the same time, taking into account the viscous torque due to the fluid motion and the electromagnetic torque developed by the image currents induced onto the shell, by the feedback currents and by the non-linear interaction between different TMs. The feedback is shown to prevent the TMs wall-locking: regardless of the amplitudes at the resonant surfaces, TMs rotate with edge values very close to those they would have in the presence of an ideal shell in the place of the resistive shell. The feedback performance and efficiency dependence on the shell characteristics will be discussed.

1. Introduction

In a magnetic confinement fusion device the presence of a conductive wall (shell) surrounding the plasma is important to guarantee magnetohydrodynamic (MHD) stability. However, the finite penetration time of the radial magnetic field of any realistic shell determines potentially dangerous MHD phenomena, among which is the wall-locking of tearing modes (TMs) [1, 2]. According to the no-slip condition [1], in the non-linear regime a m, n TM, with m and n the poloidal and toroidal mode numbers, co-rotates with the ion fluid at the resonance surface. This surface is defined by the condition $q(r_{m,n}) = m/n$. The fluid velocity is modified there by an electromagnetic torque produced by the interaction with the image currents induced into the shell by the mode rotation. Wall-locking occurs when the TM amplitude at the resonant surface exceeds a threshold, the so-called wall-locking threshold, above which the electromagnetic braking torque is large enough to determine the transition from the high frequency rotation related to the unperturbed plasma flow to a very low-frequency rotation, in which the mode is practically arrested in the laboratory frame. When this occurs the stabilizing effect of the shell is lost: the TM radial field penetrates the shell and its amplitude considerably increases. Both in tokamaks and in reversed field pinches (RFPs) this determines severe plasma–wall

interactions and can lead to premature termination of the discharges. For example, in the
RFX-mod RFP experiment [3] it is not possible to raise the plasma current above 500 kA and to
have discharges lasting more than 150 ms, with the only passive stabilization provided by a shell
whose characteristic penetration time, the shell time constant, is 0.1 s. We have to underline
that in RFX-mod the stabilizing effect of this shell on the TMs is reduced by the vacuum
vessel placed inside it, which acts like a far more resistive shell (3 ms time constant). This
additional resistive shell decreases to very low amplitudes the TMs wall-locking threshold [2].
RFX-mod has demonstrated the possibility of overcoming these limitations with the active
control of the edge radial field, made possible by a grid of active coils, placed outside the shell,
fully covering the torus. The first scheme tested the so-called intelligent shell [4], in which
the coils are coupled in a feedback scheme with the measurements provided by an identical
grid of radial field sensors, improved the plasma performances by preventing the radial field
penetration of the shell: besides a complete suppression of the resistive wall modes [5], the
TMs edge amplitude was kept at a low value. In the RFPs a certain level of amplitude for the
TMs in the non-linear regime is required by the dynamo mechanism in order to maintain the
reversed configuration [6, 7]. Therefore, these perturbations would exist even in the presence
of a perfectly conducting shell. This means that, in general, a feedback system cannot suppress
the non-linear dynamo TMs, but at best it can keep their edge amplitudes to low values. A recent
upgrade of the intelligent shell developed in RFX-mod, the clean-mode-control (CMC) [8, 9],
leads to a better control of the TMs. In fact, it fixes the TMs edge amplitudes at a value
lower than the intelligent shell. Even more importantly, it maintains the TMs into rotation for
amplitudes at the resonant surfaces that are well above the wall-locking thresholds, while with
the intelligent shell they were observed to be always stationary in the laboratory frame. Even if
these rotations occur at frequencies much smaller than the values related to the unperturbed fluid
motion, they are enough to guarantee a good spread of the power deposition onto the first wall.
The CMC is based on the real-time de-aliasing of the measurements from the high periodicity
sidebands produced by the discrete nature of the active coils: the feedback variables are not
the raw measurements as in the intelligent shell, but the poloidal and toroidal m, n Fourier
harmonics of the TMs, estimated as correctly as possible with the sideband subtraction. CMC
allows operations at 1.5 MA toroidal plasma current and discharge duration about 0.5 s [9].
The basic effects of the CMC, namely, TMs rotation and shell penetration avoidance, have
been already explained in [8] using an equilibrium model for a single TM based on the balance
between the electromagnetic torque, produced by the conductive structures and the feedback
coils surrounding the plasma, and the viscous torque due to the fluid motion. That model adopts
the standard TM formalism used in many other works (for example [2, 10]) and assumes the
multiple shells structures of RFX-mod. In this paper we present an upgrade of this equilibrium
model. In order to clarify the analysis, we treat an abstract case considering just one single
resistive shell, which therefore takes the place of the vacuum vessel also. The active coils
are assumed to be located outside it. Instead of the thin-shell approximation [11] used in [8],
a more accurate diffusion equation, which takes into account the shell thickness, is used to
describe the shell penetration [11]. The thin-shell relation can be applied in RFX-mod since,
due to the characteristics of the vacuum vessel, the TMs rotation frequencies in the presence
of feedback are not so large to invalidate this approximation. Nevertheless, in a general case
where higher frequencies are possible this approximation can fail. A more complete multi-
mode dynamic model is also developed. This model evolves the mode frequencies and edge
amplitudes of several TMs at the same time, taking into account not only the interaction with
the external structures but also the non-linear interaction between themselves. This interaction
is an important element of the TMs dynamic, since it determines the phase-locking [12], which
means that the different TMs superimpose to produce a toroidally localized coherent structure.

This dynamic model can be viewed as a generalization to non-ideal boundary conditions, i.e. resistive shell and feedback, of the phase-locking code presented in [12]. The dynamic model evolves the TMs edge amplitudes, while the amplitudes at the resonant surface are imposed, for example, from the experimental estimates. In fact, the available non-linear models for the resonant surface amplitude evolution, based on Rutherford-like approaches [13], are valid in single-helicity condition. Therefore, they are of uncertain applicability in the RFP case, where the observed dynamic involves the energy exchange between different TMs. In this case a simulation of the dynamo mechanism, which is beyond the scope of this work, would be necessary. We will show that the transition from the high frequency rotation branch to a slower branch still occurs also in the presence of CMC feedback. But, differently from the no-feedback case, the TMs rotation frequencies are also significant in the slower branch. Moreover, their edge amplitudes remain close to the values they would have in the presence of an ideal hell in the place of the resistive shell. This means that the feedback makes the resistive shell to behave close to an ideal shell, virtually for any value of the TM amplitudes at the resonant surfaces. In this case wall-locking, in the sense of mode rotation stop and shell penetration, does not occur any more. The paper is organized as follows. In section 2 the basic TM formalism is presented. The dynamic model is discussed in section 3, and the stationary single-mode limit of this model is presented in section 4. Section 5 shows the computations for a single TM performed both with the dynamic and the equilibrium models: the feedback performances and efficiency are analysed varying the gains and the shell time constant. The results so obtained are confirmed by simulations performed with the dynamic model in the presence of many TMs at the same time. The multi-mode simulations are presented in section 6. Final remarks are given in section 7. The two appendices are devoted to more technical arguments. In appendix A the formulae for the electromagnetic torque due to TMs non-linear interaction, which have been obtained in [14] with ideal boundary conditions, are presented again in the case of a resistive shell. Appendix B derives the formula for the voltages required by the feedback to the coil amplifiers.

2. Basic TM formalism

Since neither toroidal nor finite pressure effects are expected to be crucial for the problem under investigation, we describe the plasma equilibrium as a force-free cylindrical configuration, with a periodicity length $2\pi R_0$ in the z direction, with R_0 the plasma major radius: using a right-handed co-ordinate system with a simulated toroidal angle $(r, \theta, \phi \equiv z/R_0)$ the force balance condition for the equilibrium field $\boldsymbol{B}_0(r) = (0, B_{0\theta}(r), B_{0\phi}(r))$ is $\nabla \times \boldsymbol{B}_0 = \mu_0 \, \boldsymbol{J}_0 = \sigma(r)\boldsymbol{B}_0$. We assume that the plasma, whose minor radius is $r = a$, is surrounded by a single resistive shell of thickness δ_{w} and inner and outer radii, respectively, r_{wi}, $r_{\mathrm{we}} = r_{\mathrm{wi}} + \delta_{\mathrm{w}}$. The shell is assumed to be uniform; so the effects of gaps and holes are not considered in this analysis. Outside the shell at the radius $r = c$ we have a grid of active coils. The single-shell configuration is the best case to investigate all the basic aspects of the problem. The generalization to the multiple shell case will appear straightforward from the model equations we are going to introduce.

2.1. TMs representation

The same convention of [12] for the Fourier harmonics of a generic perturbed quantity $X(r, \theta, \phi, t) = \sum_{m,n \in \mathbb{Z}} x^{m,n}(r, t) \, \mathrm{e}^{\mathrm{i}(m\theta - n\phi)}$ is adopted. In the plasma and vacuum regions it is a standard procedure to represent the magnetic perturbation associated to a m, n TM in
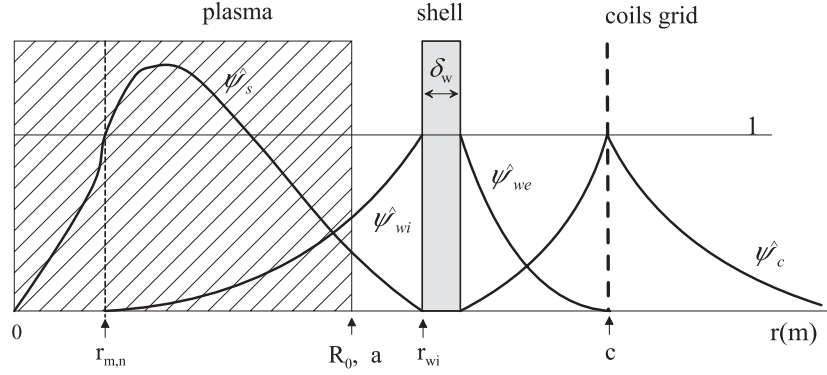
Figure 1. Layout and Newcomb's solutions splitting for each m, n mode.

terms of the mode eigenfunction

$$\psi^{m,n}(r, t) \equiv -\mathrm{i}\, r\, b_r^{m,n}(r, t) \tag{1}$$

using the linearized ideal-MHD force balance equation. This leads to a second-order ordinary differential equation in r for $\psi^{m,n}$, the so-called Newcomb's equation [15], shown in formula (A.17) of appendix A. In appendix A an equation with non-linear correction terms is also obtained (formula (A.12)), but it is not used to compute the radial profile of the perturbations, rather to derive analytical formulae which express the electromagnetic torque produced by the TMs non-linear interaction. Newcomb's equation for a m, n mode is singular at the resonant surfaces $r_{m,n}$. Likewise the solution must be interrupted into the shell region $[r_{wi}, r_{we}]$ and in correspondence to the active coils radius. For sake of simplicity the finite thickness of the coils is neglected. A standard representation is to split the Newcomb's equation solution into the sum of the different contributions obtained in the separate radial regions delimited by the magnetic axis, the resonant surface, the shell and the active coils, as shown in figure 1 [1, 8]. The continuity conditions at the resonant surface, at the coil radius and the regularity for $r \to 0$ and $r \to +\infty$ are imposed:

$$\psi^{m,n}(r, t) = \Psi_s^{m,n}(t)\, \hat{\psi}_s^{m,n}(r) + \Psi_{wi}^{m,n}(t)\, \hat{\psi}_{wi}^{m,n}(r) + \Psi_{we}^{m,n}(t)\, \hat{\psi}_{we}^{m,n}(r) + \Psi_c^{m,n}(t)\, \hat{\psi}_c^{m,n}(r);$$

$$r \notin [r_{wi}, r_{we}]. \tag{2}$$

Expression (2) is not considered inside the shell region. The complex quantities $\Psi_s^{m,n}(t)$, $\Psi_{wi}^{m,n}(t)$, $\Psi_{we}^{m,n}(t)$, $\Psi_c^{m,n}(t)$ define the amplitudes and phases of the mode at the resonant surface, at the shell inner and outer radii and at the active coils, respectively; the functions $\hat{\psi}_s^{m,n}(r)$, $\hat{\psi}_{wi}^{m,n}(r)$, $\hat{\psi}_{we}^{m,n}(r)$, $\hat{\psi}_c^{m,n}(r)$ form a real solution basis, completely determined once the equilibrium has been specified. In particular, $\hat{\psi}_s^{m,n}(r)$ is the real solution for the Newcomb's equation defined in the interval $[0, r_{wi}]$, well behaved for $r \to 0$ (it goes like $r^{|m|}$ for $m \neq 0$ and r^2 for $m = 0$), satisfying $\hat{\psi}_s^{m,n}(r_{m,n}) = 1$ and $\hat{\psi}_s^{m,n}(r_{wi}) = 0$; $\hat{\psi}_{wi}^{m,n}(r)$ is the real solution defined in the interval $[r_{m,n}, r_{wi}]$, satisfying $\hat{\psi}_{wi}^{m,n}(r_{wi}) = 1$, $\hat{\psi}_{wi}^{m,n}(r_{m,n}) = 0$; $\hat{\psi}_{we}^{m,n}(r)$ is the real solution defined in the interval $[r_{we}, c]$ satisfying $\hat{\psi}_{we}^{m,n}(r_{we}) = 1$, $\hat{\psi}_{we}^{m,n}(c) = 0$; $\hat{\psi}_c^{m,n}(r)$ is the real solution defined for $r > r_{we}$, satisfying $\hat{\psi}_c^{m,n}(c) = 1$, $\hat{\psi}_c^{m,n}(r_{we}) = 0$ and regular for $r \to +\infty$. In general, the radial derivative of the solution (2) has jumps across the resonant surface and the coil radius. These jumps are associated with the helical current sheet flowing at the resonant surface, related to the presence of a magnetic island chain, and to the coils currents, respectively. The jump at the resonant

4

surface and at the coils can be represented by

$$\Delta\Psi_{s}^{m,n} \equiv r\frac{\partial}{\partial r}\psi^{m,n}\bigg|_{r_{m,n}-}^{r_{m,n}+} = \Psi_{s}^{m,n}E_{s}^{m,n} + \Psi_{wi}^{m,n}E_{ws}^{m,n}, \tag{3}$$

$$\Delta\Psi_{c}^{m,n} \equiv r\frac{\partial}{\partial r}\psi^{m,n}\bigg|_{r_{c}-}^{r_{c}+} = \Psi_{we}^{m,n}E_{wc}^{m,n} + \Psi_{c}^{m,n}E_{c}^{m,n}, \tag{4}$$

having defined the following quantities derived by the real solution basis:

$$E_{s}^{m,n} \equiv r\frac{d}{dr}\hat{\psi}_{s}^{m,n}\bigg|_{r_{m,n}-}^{r_{m,n}+}; \qquad E_{ws}^{m,n} \equiv r\frac{d}{dr}\hat{\psi}_{wi}^{m,n}\bigg|_{r_{m,n}+}; \qquad E_{wc}^{m,n} \equiv -r\frac{d}{dr}\hat{\psi}_{we}^{m,n}\bigg|_{c-};$$

$$E_{c}^{m,n} \equiv r\frac{d}{dr}\hat{\psi}_{c}^{m,n}\bigg|_{r_{c}-}^{r_{c}+}. \tag{5}$$

Likewise, we define these further quantities, which will be used in the following:

$$E_{wi}^{m,n} \equiv -r\frac{d}{dr}\hat{\psi}_{wi}^{m,n}\bigg|_{r_{wi}-}; \qquad E_{we}^{m,n} \equiv r\frac{d}{dr}\hat{\psi}_{we}^{m,n}\bigg|_{r_{we}+};$$

$$E_{sw}^{m,n} \equiv -r\frac{d}{dr}\hat{\psi}_{s}^{m,n}\bigg|_{r_{wi}-}; \qquad E_{cw}^{m,n} \equiv r\frac{d}{dr}\hat{\psi}_{c}^{m,n}\bigg|_{r_{we}+}. \tag{6}$$

2.2. Electromagnetic torque

As discussed in appendix A, the helical current sheet flowing at a m, n resonant surface allows the formation of a dirac-like angular integrated electromagnetic torque $\delta T_{EM,\phi}^{m,n}\delta(r - r_{m,n})$, $\delta T_{EM,\theta}^{m,n}\delta(r - r_{m,n})$, where the poloidal and toroidal components stand in the ratio $\delta T_{EM,\theta}^{m,n} = -(m/n)\delta T_{EM,\phi}^{m,n}$ [1]. Ideal MHD would not allow such a torque in other regions of the plasma. The localized torque is due to two kinds of interactions: $\delta T_{EM,\phi}^{m,n} = \delta T_{EM,\phi,1}^{m,n} + \delta T_{EM,\phi,2}^{m,n}$. The first, which has already been considered in [8], involves the m, n radial field and the m, n image current induced into the resistive shell. Both quantities are affected by the m, n coils current harmonic of the feedback. As shown in appendix A this contribution is quantified by an expression involving $\Psi_{s}^{m,n}(t)$, $\Psi_{wi}^{m,n}(t)$ only (see (A.38)):

$$\delta T_{EM,\phi,1}^{m,n} = \frac{8\pi^2 R_0 n}{\mu_0}\frac{E_{ws}^{m,n}}{H^{m,n}(r_{m,n})}\text{Im}[\Psi_{wi}^{m,n}(\Psi_{s}^{m,n})^*]; \qquad H^{m,n}(r) = m^2 + n^2(r/R_0)^2. \tag{7}$$

The feedback enters in (7), since, as will be shown later, it modifies the ratio $\Psi_{wi}^{m,n}/\Psi_{s}^{m,n}$ (see formula (40)). The second is due to the non-linear interaction between TMs with different helicities. As shown in appendix A this is quantified by the expression (see equation (A.38))

$$\delta T_{EM,\phi,2}^{m,n} = \frac{8\pi^2 R_0 n}{\mu_0}\sum_{\substack{m_1,n_1,m_2,n_2 \in \mathbb{Z} \\ (m_1,n_1)+(m_2,n_2)=(m,n)}}\sum_{i,j,k\in\{s,wi\}}\text{Im}[\Psi_i^{m,n}(\Psi_j^{m_1,n_1})^*(\Psi_k^{m_2,n_2})^*]$$

$$\cdot \Gamma_{m_1,n_1,m_2,n_2}^{m,n}(i,j,k). \tag{8}$$

The real coefficients Γ are integrals of expressions containing triple products of the real Newcomb's solutions $\hat{\psi}_s(r)$, $\hat{\psi}_{wi}(r)$ for every mode involved in the non-linear interaction (see (A.39), (A.40)). Expression (8) generalizes to the resistive shell case the formula derived in [14] under the hypothesis of ideal–shell boundary condition ($\Psi_{wi} = 0$): in this case only the terms $i = j = k = s$ would be present in (8) and the non-linear interaction would represent a pure internal plasma force. Instead, since in the resistive shell case both $\Psi_s(t)$, $\Psi_{wi}(t)$ are present for every mode involved in the non-linear interaction, the torque (8) includes a component due to the external forces related to the image currents into the shell.

5

3. The dynamic model

To obtain the time evolutions of $\Psi_s^{m,n}(t)$, $\Psi_{wi}^{m,n}(t)$, $\Psi_{we}^{m,n}(t)$, $\Psi_c^{m,n}(t)$ a dynamic model has been developed. This model, besides the formulae introduced in the previous paragraph, includes

(1) the motion equation for the plasma flow, which is necessary to describe the evolution of the TMs phases at their resonant surfaces; in fact, the no-slip condition [1], in which a non-linear TM co-rotates with the ion fluid at the resonant surface, is assumed;

(2) the assumption for the TM amplitudes evolution at their resonant surfaces;

(3) the equation describing the radial field diffusion into the shell region;

(4) the equation relating the TM radial field and the current flowing into the active coils;

(5) the feedback law and the model for the coils power supply.

Now we discuss these equations in detail.

3.1. Equations of fluid motion

The electromagnetic torques, localized at the various resonant surfaces, modify the unperturbed plasma velocity profile, opposed in this action by the viscous torque. These competing effects are formalized in the single-fluid MHD motion equations for the toroidal and poloidal flux-surface averaged angular velocities $\Omega_\phi(r,t)$ and $\Omega_\theta(r,t)$ [12]:

$$\rho\frac{\partial\Omega_\phi}{\partial t} = \frac{1}{r}\frac{\partial}{\partial r}\left(\mu r\frac{\partial}{\partial r}\Omega_\phi\right) + S_\phi + \sum_{\substack{m\,\in\,\mathbb{Z}\\ n\,>\,0}}\frac{\delta T_{\mathrm{EM},\phi}^{m,n}}{4\pi^2 r R_0^3}\delta(r - r_{m,n}), \tag{9}$$

$$\rho\frac{\partial\Omega_\theta}{\partial t} = \frac{1}{r^3}\frac{\partial}{\partial r}\left(\mu r^3\frac{\partial}{\partial r}\Omega_\theta\right) - \frac{\rho}{\tau_{\mathrm{D}}}\Omega_\theta + S_\theta + \sum_{\substack{m\,\in\,\mathbb{Z}\\ n\,>\,0}}\frac{\delta T_{\mathrm{EM},\theta}^{m,n}}{4\pi^2 r^3 R_0}\delta(r - r_{m,n}) = 0. \tag{10}$$

Here μ is the plasma perpendicular viscosity, ρ is the mass density, τ_{D} is the poloidal flow damping time and S_ϕ, S_θ are phenomenological momentum source densities: for the sake of simplicity we consider all these quantities to be constant with r. The velocity boundary conditions are assumed to be

$$\frac{\partial\Omega_\phi(0,t)}{\partial r} = \frac{\partial\Omega_\theta(0,t)}{\partial r} = \Omega_\phi(a,t) = \Omega_\theta(a,t) = 0. \tag{11}$$

The summation in (9) and (10) runs over the resonant surfaces, so only the positive n are considered: the contributions of both the complex conjugate harmonics (m,n), $(-m,-n)$ for a given resonant surface are included in the electromagnetic torque expressions (7) and (8). The toroidal $\Omega_{\phi 0}(r)$ and poloidal $\Omega_{\theta 0}(r)$ angular velocities in the unperturbed state are obtained from (9) and (10) at steady state ($\partial/\partial t = 0$) discarding the electromagnetic torques. The solutions satisfying the boundary conditions (11) are

$$\Omega_{\phi 0}(r) = \frac{S_\phi}{4}\frac{\tau_{\mathrm{V}}}{\rho}\left(1 - \frac{r^2}{a^2}\right); \qquad \Omega_{\theta 0}(r) = S_\theta\frac{\tau_{\mathrm{D}}}{\rho}\left(1 - \frac{a}{r}\frac{I_1\left(\sqrt{\frac{\tau_{\mathrm{V}}}{\tau_{\mathrm{D}}}}\frac{r}{a}\right)}{I_1\left(\sqrt{\frac{\tau_{\mathrm{V}}}{\tau_{\mathrm{D}}}}\right)}\right). \tag{12}$$

Here $\tau_{\mathrm{V}} = \rho a^2/\mu$ is the viscous diffusion time. Following [12], the partial differential equations (9) and (10), with the boundary conditions (11), can be reduced into a system of

ordinary differential equations, upon defining the following set of velocity eigenfunctions and eigenvalues:

$$\frac{\mathrm{d}}{\mathrm{d}r}\left(r\mu\frac{\mathrm{d}u_j}{\mathrm{d}r}\right)+r\rho\beta_j u_j = 0; \qquad \frac{\mathrm{d}u_j(0)}{\mathrm{d}r}=u_j(a)=0, \tag{13}$$

$$\frac{\mathrm{d}}{\mathrm{d}r}\left(r^3\mu\frac{\mathrm{d}v_j}{\mathrm{d}r}\right)+r^3\rho\gamma_j v_j = 0; \qquad \frac{\mathrm{d}v_j(0)}{\mathrm{d}r}=v_j(a)=0. \tag{14}$$

From (13) one gets

$$u_j(r)=C_j J_0\left(\frac{r}{a}j_{0,j}\right); \qquad \beta_j = \frac{j_{0,j}^2}{\tau_{\mathrm{V}}}, \tag{15}$$

where $j_{0,j}$ is the jth positive zero of the Bessel function J_0. Upon defining $C_j = (\int_0^a r(J_0((r/a)j_{0,j}))^2\,\mathrm{d}r)^{-1/2}$ we satisfy the orthonormality relation

$$\int_0^a r u_j(r)u_k(r)\,\mathrm{d}r = \delta_{j,k}. \tag{16}$$

From (14) we get

$$v_j(r)=E_j\frac{J_1\left(\frac{r}{a}j_{1,j}\right)}{r}; \qquad \gamma_j = \frac{j_{1,j}^2}{\tau_{\mathrm{V}}}, \tag{17}$$

where $j_{1,j}$ is the jth positive zero of the Bessel function J_1. Upon defining $E_j = (\int_0^a r(J_1((r/a)j_{1,j}))^2\,\mathrm{d}r)^{-1/2}$ we satisfy the orthonormality relation

$$\int_0^a r^3 v_j(r)v_k(r)\,\mathrm{d}r = \delta_{j,k}. \tag{18}$$

According to the Sturm–Liouville theory the eigenfunctions u_j, v_j form two complete sets, so we can expand the toroidal and poloidal angular velocities as

$$\Omega_\phi(r,t)=\sum_{j=1,+\infty} g_j(t)u_j(r); \qquad \Omega_\theta(r,t)=\sum_{j=1,+\infty} f_j(t)v_j(r). \tag{19}$$

Note that the boundary conditions (11) are automatically satisfied. Using the orthonormality relations (16) and (18), the partial differential equations (9) and (10) simplify to a numerable set of ordinary differential equations for the functions $g_j(t)$, $f_j(t)$:

$$\rho\frac{\mathrm{d}g_j}{\mathrm{d}t}=-\rho\frac{j_{0,j}^2}{\tau_{\mathrm{V}}}g_j + S_\phi\int_0^a r u_j(r)\,\mathrm{d}r + \sum_{\substack{m\,\in\,\mathbb{Z}\\ n\,>\,0}}\frac{u_j(r_{m,n})}{4\pi^2 R_0^3}[\delta T_{\mathrm{EM},\phi,1}^{m,n}+\delta T_{\mathrm{EM},\phi,2}^{m,n}]$$

$$j=1,...,j_{\max}, \tag{20}$$

$$\rho\frac{\mathrm{d}f_j}{\mathrm{d}t}=-\rho\frac{j_{1,j}^2}{\tau_{\mathrm{V}}}f_j - \frac{\rho f_j}{\tau_{\mathrm{D}}} + S_\theta\int_0^a r^3 v_j(r)\,\mathrm{d}r - \sum_{\substack{m\,\in\,\mathbb{Z}\\ n\,>\,0}}\frac{m}{n}\frac{v_j(r_{m,n})}{4\pi^2 R_0}[\delta T_{\mathrm{EM},\phi,1}^{m,n}+\delta T_{\mathrm{EM},\phi,2}^{m,n}]$$

$$j=1,...,j_{\max}. \tag{21}$$

For practical evaluations, the system (20) and (21) is truncated to a finite order $j_{\max}$.

3.2. Perturbations at the resonant surfaces

The dynamo TMs are assumed to be in the non-linear regime. Their amplitudes and phases at the resonant surfaces are defined by

$$\Psi_s^{m,n}(t) = \Psi_{s0}^{m,n}(t)e^{i\varphi^{m,n}(t)}. \tag{22}$$

As explained in the introduction we do not model the amplitude evolution, so $\Psi_{s0}^{m,n}(t)$ are imposed (for example, from the experimental estimates). Instead, the phases are evolved with the no-slip condition [1], according to which a TM co-rotates with the ion fluid at the resonant surface:

$$\frac{d\varphi^{m,n}}{dt} = n\Omega_\phi(r_{m,n}, t) - m\Omega_\theta(r_{m,n}, t) = \sum_{j=1,+\infty} [ng_j(t)u_j(r_{m,n}) - mf_j(t)v_j(r_{m,n})]. \tag{23}$$

3.3. Perturbations inside the shell

Assuming $\delta_w \ll r_{wi}$, and neglecting the curvature terms, the evolution of the m, n perturbations inside the shell are governed by the following parabolic equations [11]:

$$\mu_0\sigma\frac{\partial\psi^{m,n}}{\partial t} = \frac{\partial^2\psi^{m,n}}{\partial r^2}; \qquad r \in [r_{wi}, r_{we}], \tag{24}$$

where σ is the shell conductivity. The shell time constant is $\tau_w = \mu_0 r_{wi}\delta_w\sigma$. Equation (24) is more general than the thin-shell dispersion relation $\tau_w (\partial\psi^{m,n}/\partial t)|_{r_{wi}} = r_{wi} (\partial\psi^{m,n}/\partial r)|_{r_{wi}}^{r_{we}}$, often used in this kind of analysis [8, 10], which is valid only in the frequency range $\delta_w/r_{wi} \ll \omega\tau_w \ll r_{wi}/\delta_w$, where there is virtually no radial variation of the perturbation inside the shell. Equation (24) needs two boundary conditions at the shell inner and outer radii. They are imposed on the radial derivative of the perturbations, matching the solution of (24) to Newcomb's equation solution. Making use of the definitions (6) we have

$$\frac{\partial}{\partial r}\psi^{m,n}\bigg|_{r_{wi}} = -\frac{1}{r_{wi}}(\Psi_s^{m,n}E_{sw}^{m,n} + \Psi_{wi}^{m,n}E_{wi}^{m,n}); \tag{25}$$

$$\frac{\partial}{\partial r}\psi^{m,n}\bigg|_{r_{we}} = \frac{1}{r_{we}}(\Psi_{we}^{m,n}E_{we}^{m,n} + \Psi_c^{m,n}E_{cw}^{m,n}). \tag{26}$$

3.4. Perturbations at the coils

The quantity $\Psi_c^{m,n}(t)$ is expressed in terms of $\Psi_{we}^{m,n}$ and the coils current m, n discrete Fourier harmonic $I_c^{m,n}$ combining equation (4) with another expression for the derivative discontinuity at the coils radius obtained from Ampere's law [17]:

$$\Delta\Psi_c^{m,n} = L^{m,n}I_c^{m,n}; \qquad I_c^{m,n} = \frac{1}{NM}\sum_{\substack{i=1,M \\ j=1,N}}I_{i,j}e^{-i(m\theta_i-n\phi_j)},$$

$$L^{m,n} = i\mu_0 H^{m,n}(c)\frac{\sin\left(n\dfrac{\Delta\phi}{2}\right)}{n\dfrac{\Delta\phi}{2}}\frac{\sin\left(m\dfrac{\Delta\theta}{2}\right)}{m\dfrac{\Delta\theta}{2}}. \tag{27}$$

Here the active coils are supposed to be N_c-turn rectangular loops with poloidal and toroidal extent $\Delta\theta = 2\pi/M$ and $\Delta\phi = 2\pi/N$, respectively, forming a M(poloidal)$\times N$(toroidal) grid fully covering the torus. For sake of simplicity the finite thickness of the coils is neglected. $I_{i,j}$ is the total current flowing in the i, j coil, and the anticlockwise direction looking from above is taken to be the positive versus.

3.5. Feedback law and active coil power supply model

The dynamic model is closed by the equation for $I_c^{m,n}$, which is obtained by prescribing the feedback law and modelling the coils power supply. The feedback law determines the reference current harmonics $I_{ref}^{m,n}$: here we use the CMC scheme, implemented as a standard P.D. controller applied to the m, n radial field harmonics at a given control radius r_f between the plasma edge and the inner shell surface $a \leqslant r_f \leqslant r_{wi}$. These harmonics are possibly obtained by extrapolating the measurements as described in [8]. As discussed in the introduction, this is the feedback scheme which in RFX-mod has been proven to be more efficient on TMs. If $K_p^{m,n}$, $K_d^{m,n}$ are, respectively, the proportional and derivative gains applied to the m, n mode, the CMC law is

$$I_{ref}^{m,n} = \frac{r_f}{\mu_0} \left(K_p^{m,n} w_r^{m,n} + K_d^{m,n} \frac{d}{dt} w_r^{m,n} \right). \tag{28}$$

To be realistic as much as possible we have modelled the measured radial field harmonics as a filtered version of the true ones:

$$\tau_d \frac{d}{dt} w_r^{m,n} + w_r^{m,n} = b_r^{m,n}(r_f, t), \tag{29}$$

$$b_r^{m,n}(r_f, t) = \frac{i}{r_f} [\Psi_s^{m,n}(t) \hat{\psi}_s^{m,n}(r_f) + \Psi_{wi}^{m,n}(t) \hat{\psi}_{wi}^{m,n}(r_f)]. \tag{30}$$

The parameter τ_d quantifies both the filters that must be applied in order to avoid the aliasing in the frequency domain during the digital acquisition of the signals, and the delay introduced by the feedback operations, for example, the real-time Fourier analysis. In this model we imagine that dw_r/dt is the signal acquired by the feedback, while w_r is obtained by integration (this is different from RFX-mod, where the feedback system acquires w_r and obtains dw_r/dt by a numerical derivative which requires an additional filter [8]). In (28) the gains are negative (or have a negative real part if they are complex), so the radial field generated by the coils, which is in-phase with the current, opposes the measured one. We neglect the integral control in (28), since it has not proven to be effective for the TMs control in RFX-mod [8, 9]. The reason is that TMs tends to rotate, so the integral control introduces an undesirable delay. In this formulation we assume that the m, n Fourier harmonics can be correctly evaluated, possibly de-aliasing the measurements from the high periodicity sidebands $(m + lM, n + pN)$, $l, p \in Z$ produced by the discrete nature of the active coils. The aliasing effect can be reduced to negligible levels if the sensors and the active coils have different periodicities in poloidal and toroidal directions. If the periodicity is identical, [8] has shown that it is possible to give a good estimate of the coil sidebands using the currents measurements and to subtract them from the radial field measurements in real time. The sidebands do not correspond to any unstable plasma mode if M, N are large enough (condition assumed in this model). Therefore, they are not expected to interact significantly with the dynamo TMs, and they are not considered in this model. Due to the unavoidable delay of the coils power supplies, the actual current harmonics in the coils $I_c^{m,n}$ do not coincide with the reference harmonics $I_{ref}^{m,n}$. In RFX-mod, the relationship between the two quantities can be modelled by a one-pole filter law [18]:

$$\tau_c \frac{d}{dt} I_c^{m,n} + I_c^{m,n} = I_{ref}^{m,n}. \tag{31}$$

In fact the active coils power supplies have an internal feedback controller that can be represented by the scheme reported in figure 2: K denotes a proportional gain, $V_c^{m,n}$ is the discrete Fourier transform of the voltage applied to the coil and $G(i\omega)$ is the transfer function between voltage and current, which can be approximated by a one-pole filter law. Therefore, the global transfer function between $I_c^{m,n}$ and $I_{ref}^{m,n}$ is still a one-pole filter law, with the pole τ_c depending on the gain K. Equation (31) will be adopted by our model.
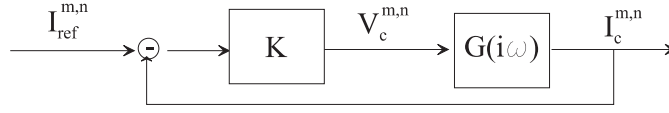
Figure 2. Scheme of the global transfer function of the active coils power supply in RFX-mod.

3.6. Feedback performances and efficiency

In an RFP the dynamo TMs would exist even with an ideal shell at the plasma edge $r = a$. While a certain level of radial field at the resonant surface is required by the dynamo mechanism, the feedback should try to mimic an ideal shell placed at $r = a$ reducing as small as possible the radial field there. Therefore, we take the absolute value of the ratio between the radial field amplitudes at the plasma edge and at the resonant surface $\hat{b}_a^{m,n} \equiv |b_r^{m,n}(a)/b_r^{m,n}(r_{m,n})|$ as a merit parameter to quantify the feedback performances. An efficient feedback should keep at a low value the edge radial field, without demanding too much power for the coil amplifiers. The power is obtained combining the coils current and voltages. The coils voltages are computed with an equation derived in appendix B, where it is shown that the m, n discrete Fourier harmonics (defined in (27)) of the currents and the voltages are related by

$$V_c^{m,n} = \frac{R_c}{N_c} I_c^{m,n} + l^{m,n} \frac{\mathrm{d}}{\mathrm{d}t} I_c^{m,n} - \frac{4 R_0 N_c}{mn} \sin\left(n \frac{\Delta\phi}{2}\right) \sin\left(m \frac{\Delta\theta}{2}\right) \frac{\mathrm{i} E_{wc}^{m,n}}{E_c^{m,n}} \frac{\mathrm{d}}{\mathrm{d}t} \Psi_{we}^{m,n}. \qquad (32)$$

Here $l^{m,n}$ are effective inductances and R_c is the resistance of the coil. The second and third terms provide the time variation of the radial flux enclosed by the coils. The inductances $l^{m,n}$ also contain the contribution of the coil generated sidebands evaluated using the vacuum approximation.

3.7. Summary

In conclusions, our dynamic model is a system of parabolic PDE (24) for every mode considered, with boundary conditions (25) and (26), coupled with algebraic relations (4) and (27), with a system of ODE represented by equations (7), (8), (20)–(23), (28)–(31) and with relation (32). It is a non-linear model since both expressions (7) and (8) for the electromagnetic torque are non-linear. It is solved using a FORTRAN 90 program, which implements the NAG routine 'nag_pde_parab_1d_fd'. The real quantities (5) and (6) are obtained solving Newcomb's equation (A17) for a given equilibrium using the NAG routine 'nag_rk_interval'. The outputs are the variables g_j, f_j, $j = 1, \ldots, j_{\max}$, and $\varphi^{m,n}$, $\Psi_{wi}^{m,n}$, $\Psi_{we}^{m,n}$, $\Psi_c^{m,n} I_c^{m,n}$, $w_r^{m,n}$, $V_c^{m,n}$ for every mode considered. The system of equations is initialized with zero magnetic perturbations, coils currents, fluid velocity and giving random phases for the modes. The momentum sources in equation (20) and (21) are determined from relationship (12) with the unperturbed velocity profiles, providing a value for $\Omega_{\phi 0}(r)$ and $\Omega_{\theta 0}(r)$ at a given radius.

4. The stationary single-mode model

It is also interesting to study the problem in a simpler situation, without the non-linear interaction between different TMs, by considering a single m, n TM. If its amplitude at the resonant surface $\Psi_{s0}^{m,n}$ has a constant value, the solution of the previous system of equations approaches, in general, a stationary state in which the fluid velocity profile is constant, the mode rotates with constant frequency $\mathrm{d}\varphi^{m,n}/\mathrm{d}t = \omega$ and the time dependence reduces to $\mathrm{e}^{\mathrm{i}\omega t}$ for all the quantities $\Psi_{wi}^{m,n}$, $\Psi_{we}^{m,n}$, $\Psi_c^{m,n} I_c^{m,n}$, $w_r^{m,n}$, $V_c^{m,n}$. In this case the model provides a

non-linear algebraic equation for the equilibrium frequency ω, which we are going to derive. This equation has already been obtained in [8] using the thin-shell relation. Here we present an upgraded version, since we are considering the more accurate diffusion equation (24). This model provides a useful comparison with the dynamic model. In stationary conditions, in the presence of a single mode, the motion equations (9) and (10) reduce to

$$\frac{1}{r}\frac{\mathrm{d}}{\mathrm{d}r}\left(\mu r \frac{\mathrm{d}}{\mathrm{d}r}\Delta\Omega_\phi\right) + \frac{\delta T^{m,n}_{\mathrm{EM},\phi,1}}{4\pi^2 r R_0^3}\delta(r - r_{m,n}) = 0 \quad , \tag{33}$$

$$\frac{1}{r^3}\frac{\mathrm{d}}{\mathrm{d}r}\left(\mu r^3 \frac{\mathrm{d}}{\mathrm{d}r}\Delta\Omega_\theta\right) - \frac{\rho}{\tau_\mathrm{D}}\Delta\Omega_\theta - \frac{m}{n}\frac{\delta T^{m,n}_{\mathrm{EM},\phi,1}}{4\pi^2 r^3 R_0}\delta(r - r_{m,n}) = 0, \tag{34}$$

having defined as $\Delta\Omega_\phi(r) \equiv \Omega_\phi(r) - \Omega_{\phi 0}(r)$, $\Delta\Omega_\theta(r) \equiv \Omega_\theta(r) - \Omega_{\theta 0}(r)$ the difference between the velocity profiles in the final stationary state and the unperturbed profiles; (33) and (34) are solved in the two regions $0 < r < r_{m,n}$, $r_{m,n} < r < a$, with the boundary conditions $\Delta\Omega'_\phi(0) = \Delta\Omega'_\theta(0) = \Delta\Omega_\phi(a) = \Delta\Omega_\theta(a) = 0$ and imposing the continuity of the solution at $r = r_{m,n}$. The discontinuities of the radial derivative $\Delta\Omega'_\phi$, $\Delta\Omega'_\theta$ across the resonant surface produce the angular integrated viscous torques, which balance the electromagnetic torque. It is possible to show that

$$-4\pi^2 R_0^3 \mu \Delta\Omega_\phi(r_{m,n}) \Big/ \ln\left(\frac{a}{r_{m,n}}\right) + \delta T^{m,n}_{\mathrm{EM},\phi,1} = 0, \tag{35}$$

$$4\pi^2 R_0 r_{m,n}^2 \mu \Delta\Omega_\theta(r_{m,n}) \, F\left(\sqrt{\frac{\tau_\mathrm{V}}{\tau_\mathrm{D}}}\right) + \frac{m}{n}\delta T^{m,n}_{\mathrm{EM},\phi,1} = 0, \tag{36}$$

where

$$F(x) = \frac{I_1(x)}{I_1(x(r_{m,n}/a))[K_1(x(r_{m,n}/a))I_1(x) - I_1(x(r_{m,n}/a))K_1(x)]}$$

is a positive function. At the stationary state the no-slip condition (23) is $\omega = n\Omega_\phi(r_{m,n}) - m\Omega_\theta(r_{m,n})$, and defining the unperturbed frequency $\omega_0 \equiv n\Omega_{\phi 0}(r_{m,n}) - m\Omega_{\theta 0}(r_{m,n})$, the combination of (7), (35) and (36) provides

$$\frac{2\Im^{m,n} E^{m,n}_{\mathrm{ws}}}{r_{m,n}^2 H^{m,n}(r_{m,n})}\mathrm{Im}[\Psi^{m,n}_{\mathrm{wi}}(\Psi^{m,n}_{\mathrm{s}})^*] + \omega_0 - \omega = 0, \tag{37}$$

where $\Im^{m,n} = (\mu_0\mu)^{-1} \cdot [n^2(r_{m,n}/R_0)^2 \ln(a/r_{m,n}) + m^2 F(\sqrt{\tau_\mathrm{V}/\tau_\mathrm{D}})^{-1}]$. To get the desired equation, we have to express $\Psi^{m,n}_{\mathrm{wi}}$ in terms of $\Psi^{m,n}_{\mathrm{s}}$ and ω in (37). Being the time dependence $\mathrm{e}^{\mathrm{i}\omega t}$, the resistive shell diffusion equation (24) becomes

$$\frac{\partial^2 \psi^{m,n}}{\partial r^2} = \left(\frac{2\gamma}{\delta_\mathrm{w}}\right)^2 \psi^{m,n}; \qquad \gamma = \frac{1}{2}\left(\frac{\mathrm{i}\omega\tau_\mathrm{w}\delta_\mathrm{w}}{r_{\mathrm{wi}}}\right)^{1/2}; \qquad r \in [r_{\mathrm{wi}}, r_{\mathrm{we}}] \tag{38}$$

with solution

$$\psi^{m,n} = \frac{\Psi_{\mathrm{we}} + \Psi_{\mathrm{wi}}}{2\cosh(\gamma)}\cosh\left[\left(\frac{2\gamma}{\delta_\mathrm{w}}\right)(r - r_\mathrm{w})\right] + \frac{\Psi_{\mathrm{we}} - \Psi_{\mathrm{wi}}}{2\sinh(\gamma)}\sinh\left[\left(\frac{2\gamma}{\delta_\mathrm{w}}\right)(r - r_\mathrm{w})\right];$$

$$r_\mathrm{w} = \frac{r_{\mathrm{wi}} + r_{\mathrm{we}}}{2}. \tag{39}$$

Inserting (39) in the l.h.s of the boundary conditions (25) and (26), and combining the ensuing equations with (4), (27)–(31) , we get

$$\Psi^{m,n}_{\mathrm{wi}} = B^{m,n}(\omega, K^{m,n}_\mathrm{p}, K^{m,n}_\mathrm{d})\Psi^{m,n}_{\mathrm{s}}, \tag{40}$$

11

$$B(\omega, K_{\rm p}, K_{\rm d}) = \left[E_{\rm sw}E_{\rm c} + \frac{r_{\rm wi}}{r_{\rm we}}\frac{E_{\rm cw}\chi_{\rm s}(\omega, K_{\rm p}, K_{\rm d})}{\cosh(2\gamma)} + \frac{\delta_{\rm w}}{r_{\rm we}}\frac{\tanh(2\gamma)}{2\gamma}E_{\rm sw}(E_{\rm cw}E_{\rm wc} - E_{\rm c}E_{\rm we}) \right]$$

$$\cdot \left[{\rm i}\omega\tau_{\rm w}\frac{\tanh(2\gamma)}{2\gamma}E_{\rm c} - G_{\rm wc} - \frac{r_{\rm wi}}{r_{\rm we}}\frac{E_{\rm cw}\chi_{\rm wi}(\omega, K_{\rm p}, K_{\rm d})}{\cosh(2\gamma)} \right.$$

$$\left. + \frac{\delta_{\rm w}}{r_{\rm we}}\frac{\tanh(2\gamma)}{2\gamma}E_{\rm wi}(E_{\rm c}E_{\rm we} - E_{\rm cw}E_{\rm wc}) \right]^{-1}, \tag{41}$$

$$\chi_{\rm s}^{m,n} = \frac{{\rm i}L^{m,n}\hat{\psi}_{\rm s}^{m,n}(r_{\rm f})}{\mu_0}\frac{K_{\rm p}^{m,n} + {\rm i}\omega K_{\rm d}^{m,n}}{(1 + {\rm i}\omega\tau_{\rm c})(1 + {\rm i}\omega\tau_{\rm d})},$$

$$\chi_{\rm wi}^{m,n} = \frac{{\rm i}L^{m,n}\hat{\psi}_{\rm wi}^{m,n}(r_{\rm f})}{\mu_0}\frac{K_{\rm p}^{m,n} + {\rm i}\omega K_{\rm d}^{m,n}}{(1 + {\rm i}\omega\tau_{\rm c})(1 + {\rm i}\omega\tau_{\rm d})}, \tag{42}$$

$$G_{\rm wc}^{m,n} = \left(E_{\rm wi}^{m,n} + \frac{r_{\rm wi}}{r_{\rm we}}E_{\rm we}^{m,n} \right)E_{\rm c}^{m,n} - \frac{r_{\rm wi}}{r_{\rm we}}E_{\rm cw}^{m,n}E_{\rm wc}^{m,n}. \tag{43}$$

In (41) we have dropped the m, n superscript for ease of notation. Inserting (40) in (37), the torque balance relation becomes the following non-linear equation for ω:

$$T(\omega) \equiv \frac{1}{2}\left(\frac{2\Psi_{\rm s0}^{m,n}}{r_{m,n}} \right)^2 \frac{\Im^{m,n}E_{\rm ws}^{m,n}}{H^{m,n}(r_{m,n})}{\rm Im}[B^{m,n}(\omega, K_{\rm p}^{m,n}, K_{\rm d}^{m,n})] + \omega_0 - \omega = 0;$$

$$\partial T/\partial\omega|_{T=0} < 0. \tag{44}$$

The constraint of the derivative of $T(\omega)$ selects the stable equilibrium solutions; $2 \times \Psi_{\rm s0}$ represents the global mode amplitude at the resonant surface, taking into account the complex conjugate contribution also. Once this amplitude, the feedback gains and the plasma flow parameters μ, $\tau_{\rm D}$, ρ, ω_0 are set, equation (44) provides the equilibrium frequency ω. Newcomb's solution (2) is then fully determined, since not only $\Psi_{\rm wi}^{m,n}$ but also $\Psi_{\rm we}^{m,n}$, $\Psi_{\rm c}^{m,n}$ can be obtained with relations similar to (40). Equation (44) is solved using a Fortran 90 program, which implements the NAG routine 'nag_nlin_eqn_sol'.

5. Single-mode analysis

To understand the basic aspect of the feedback on TMs we start considering just one single m, n mode, using both the stationary model and the dynamic model. In this case the dynamic model is solved with $\delta T_{{\rm EM},\phi,1}^{m,n}$ as the only contribution to the electromagnetic torque in equations (20) and (21). This section will be devoted to the computation for the $m = 1$, $n = 7$ TM, which in RFX-mod is the innermost resonant and the most important one in the high current regime.

5.1. Layout, fluid and equilibrium parameters

These preliminary considerations are valid both for the single-mode and the multi-mode analyses, which will be presented in section 6. We take the same geometrical parameter and the active coils grid characteristic of RFX-mod: $a = 0.459$ ms, $R_0 = 2$ m, $c = 0.5815$ m, $M = 4$, $N = 48$, $N_{\rm c} = 60$, $R_{\rm c} = 0.8\,\Omega$. In equation (31) we take the RFX-mod value for the pole of the coils power supplies transfer function, obtained after the optimization of the relative internal feedback loop [18]: $\tau_{\rm c} = 0.5$ ms. In equation (29) the parameter $\tau_{\rm d}$ is assumed to be a fraction of $\tau_{\rm c}$: $\tau_{\rm d} = 0.1$ ms. It does not seem reasonable to impose a smaller value, since $\tau_{\rm d}$ also incorporates the delay introduced by the feedback real-time computations.

In RFX-mod an Inconel shell (the vacuum vessel) with $\tau_w = 3$ ms is placed just behind the graphite tiles at $r_{wi} = 0.475$ m, and a copper shell with $\tau_w = 0.1$ s and $\delta_w = 3$ mm is placed outside it at $r_{wi} = 0.5125$ m. Instead, in this analysis a single shell is considered. If not otherwise specified, this shell is assumed to be placed just behind the graphite tiles at $r_{wi} = 0.475$ m. We do not perform a complete scan of the two parameters, conductivity and thickness, which characterize the shell. Rather, we perform a scan with the shell time constant according to the following considerations. Copper is the most conductive metal available to build a shell. Therefore to have $\tau_w \geqslant 0.1$ s we take a copper shell with thickness $\delta_w = \tau_w(s)/0.1 \times 3$ mm, with the limit value $\tau_w = 0.3$ s, since equation (24) holds only for $\delta_w \ll r_{wi}$. Instead, to have $\tau_w < 0.1$ s we keep $\delta_w = 3$ mm, since reducing further the thickness of a single shell seems hardly feasible from the mechanical point of view, and we imagine that the shell is made of a material less conductive than copper. The fluid and equilibrium parameters are imposed from the RFX-mod experiment whenever possible and fixed with sensible hypothesis in the absence of reliable determinations. The magnetic equilibrium ($\alpha = 6$, $\theta_0 = 1.44$ for the current profile parametrization according to equation (A.1) in appendix A; $I_p = 1.45$ MA for the toroidal plasma current) is derived from a typical high current shot of RFX-mod (#23810). An important fluid parameter is the plasma perpendicular viscosity. To our knowledge, the viscosity in an RFP has been measured in MST only, perturbing the plasma velocity profile by a biased electrode [19]. From the flow damping the perpendicular viscosity was inferred to be anomalous: $\mu/\rho \approx 50$ m^2 s^{-1}. For RFX-mod this value would provide a viscous diffusion time $\tau_V = \rho a^2/\mu \approx 4$ ms. Taking into account the similar geometrical dimensions of MST and RFX-mod, we assume $\tau_V = 4$ ms. The viscosity μ is determined taking for the electron particles density the value $n_e = 3 \times 10^{19}$ m^{-3} of the reference shot. Another unknown quantity in RFX-mod is the unperturbed flow velocity, which in our model fixes the momentum sources via equations (12). In RFX-mod we have measurements of some impurities velocity in the intermediate/external region of the plasma ($r/a > 0.6$). In particular the CV toroidal velocity is considered to be representative of the toroidal flow of the main ion [20]. However, these measurements cannot be taken as the unperturbed velocity profile, since in RFX-mod the plasma flow is always modified by the fact that the TMs are locked to the wall (in the absence of feedback) or rotating at a frequency smaller than the unperturbed value (with feedback). Instead in MST, in which TMs for low amplitudes can rotate at their natural frequencies, the unperturbed toroidal velocity of the CV impurity ions has been measured to be about 15 Km s^{-1} at $r/a \approx 0.4$ [19]. Therefore in our computations we impose the value $\Omega_{\phi 0}(a/2) = 1.5 \times 10^4/R_0$(rad s^{-1}) for the unperturbed toroidal angular velocity at half plasma radius. Concerning the unperturbed poloidal velocity, imposing $\Omega_{\theta 0}(a/2) = 3500/(a/2)$(rad s^{-1}) and $\tau_D = \tau_V$, the final perturbed velocity profile, computed by the dynamic model with the non-linear interaction between all the relevant TMs, is compatible with the RFX-mod CV measurements mentioned above. This will be discussed in section 6. Finally, the system of equations (20) and (21) is truncated with $j_{max} = 50$: we have verified that increasing further the number of eigenfunctions u_j, v_j does not lead to appreciable variations in the result.

5.2. Wall-locking avoidance

In figure 3 we show the dynamic model solution obtained with no feedback ($K_p^{m,n} = 0$, $K_d^{m,n} = 0$), for a $\tau_w = 0.1$ s shell, imposing for the radial field amplitude at the resonant surface $b_{rs}^{m,n} = \Psi_{s0}^{m,n}/r_{m,n}$ a linear ramp from 0 up to 15 mT lasting 0.12 s: for every value of b_{rs} the mode frequency and the ratio $\hat{b}_a^{m,n}$ are reported. The mode frequency starts from zero and reaches the value corresponding to the unperturbed velocity profile ($\omega_0 = 44\,970$ rad s^{-1})
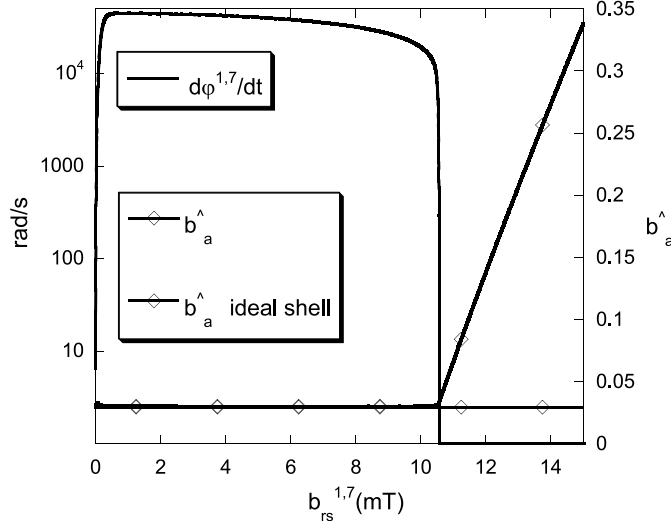
Figure 3. Dynamic computation for the $m = 1$, $n = 7$ TM without feedback taking $\tau_w = 0.1$ s: b_{rs} ramps linearly from 0 to 15 mT in 0.12 s. The value of $\hat{b}_a^{m,n}$, with an ideal shell in the place of the resistive shell, is also shown.

after a time τ_V. It decreases gradually while the mode amplitude increases, but when the latter exceeds the wall-locking threshold, which is about $b_{rs} \approx 10$ mT for the chosen value of τ_w, the frequency drops at such low values that the mode is practically arrested in the laboratory frame. While in the high frequency branch the shell behaves approximately like an ideal shell, in the low frequency branch its stabilizing effect is lost, and the radial field penetrates it, since the ratio $\hat{b}_a^{m,n}$ increases departing from the ideal-shell value. The wall-locking threshold dependence on τ_w is shown in figure 4. The numerical computation is performed with the stationary model in the absence of feedback. Here this threshold is called the high–low b_{h-l} frequency threshold for reasons that will be clear in the following. The saturation of b_{h-l} for $\tau_w > 0.1$ s agrees with the dependence $(\tau_w/\delta_w)^{1/4}$ of the analytical formula derived in [2] in the so-called thick-shell asymptotic regime (remember our assumption of a copper shell, i.e. $\tau_w/\delta_w = $ const for $\tau_w > 0.1$ s). Numerical computations performed with both the dynamic and the stationary models show that the feedback weakly affects the high–low frequency threshold b_{h-l}. Nevertheless, the feedback radically changes the properties of the solution when the amplitude is above b_{h-l}. This is shown in the next two figures 5 and 6 considering three feedback simulations with the dynamic model for the same b_{rs} ramp of figure 3: the simulations differ for the shell time constant τ_w or the control radius r_f according to the figure captions. The symbols superimposed to the three curves are the equilibrium solutions computed by the stationary model for the same values of b_{rs}. The gains set in the three cases are chosen after a scan, which will be discussed later. Note that the imposed derivative gain $K_d = \tau_c K_p$ is the value which compensates in equation (28) the pole in the coils transfer function (31). Figure 5 shows that when the amplitude is above b_{h-l} there is still the transition from the high to the low-frequency branch. But, in the presence of feedback the mode rotation is also significant in the low-frequency branch. Moreover, figure 6 shows that $\hat{b}_a^{m,n}$ remains close to the ideal-shell value, even in the low-frequency branch of the solution. Note that there is very good agreement between the stationary computation and the dynamic model solution. The agreement is not perfect, due to the continuous variation of b_{rs} during the imposed ramp in
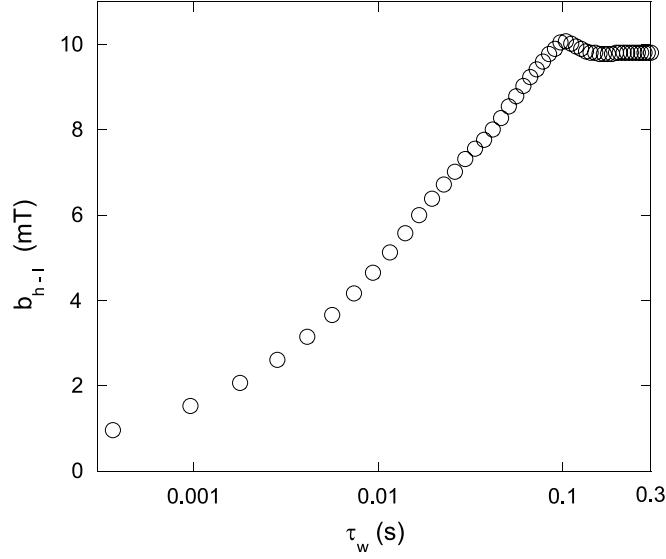
Figure 4. High–low frequency threshold b_{h-l} given by the stationary model in the case without feedback. Note the logarithmic scale in the x-axis.

the dynamic computation. Nonetheless, this demonstrates that for a constant b_{rs} the feedback determines a true equilibrium condition in which the mode rotates with constant frequency and $\hat{b}_a^{m,n}$. In this case the wall-locking, in the sense of rotation stop and shell penetration for amplitudes above b_{h-l}, as shown in figure 3, is avoided. This is the reason for which we have renamed the b_{h-l} threshold. In figure 6 it can be noted that the dependence of $\hat{b}_a^{m,n}$ on b_{rs} is negligible even in the low-frequency branch. This is confirmed by further extending the b_{rs} scan in the low-frequency branch as shown in figure 7. The conclusion is that the feedback (for given value of the gains, control radius and shell characteristics) fixes not the absolute value of the edge radial field, but the ratio $\hat{b}_a^{m,n}$. In other words, the feedback determines the mode eigenfunction profile. Note that the feedback performances in terms of $\hat{b}_a^{m,n}$ are better in the $\tau_w = 0.1$ s case than in the $\tau_w = 3$ ms case: the time constant dependence will be further investigated in section 5.5. Moving the feedback radius from $r_f = r_{wi}$ to $r_f = a$ does not appreciably improve the feedback performances. On the other hand, the control at $r_f = a$ is less efficient, since the voltage and currents required to the coils are higher: this is shown in figure 8 plotting the product $|V_c^{m,n} \cdot I_c^{m,n}|/N_c$, which represents an estimate of the maximum power required to the coils (in the power expression the voltage must multiply the current flowing in each turn of the coil; this is the reason for dividing the total coils currents by N_c). The feedback dependence on the control radius will be further investigated in section 5.4. Also note that passing from $\tau_w = 0.1$ s to $\tau_w = 3$ ms with the same control radius $r_f = r_{wi}$ makes the feedback less efficient.

5.3. Gains dependence for the control radius at $r_f = r_{wi}$

We now want to study the feedback performance and efficiency dependence on the gains in the low frequency branch keeping $r_f = r_{wi}$. The shell time constant is set at $\tau_w = 0.1$ s. The imposed mode amplitude at the resonant surface is $b_{rs}(mT) = 12 \times [1 - \exp(-2000 \times t(s))]$, which mimics a fast exponential growth followed by a saturation at a value above b_{h-l}. Figures 9
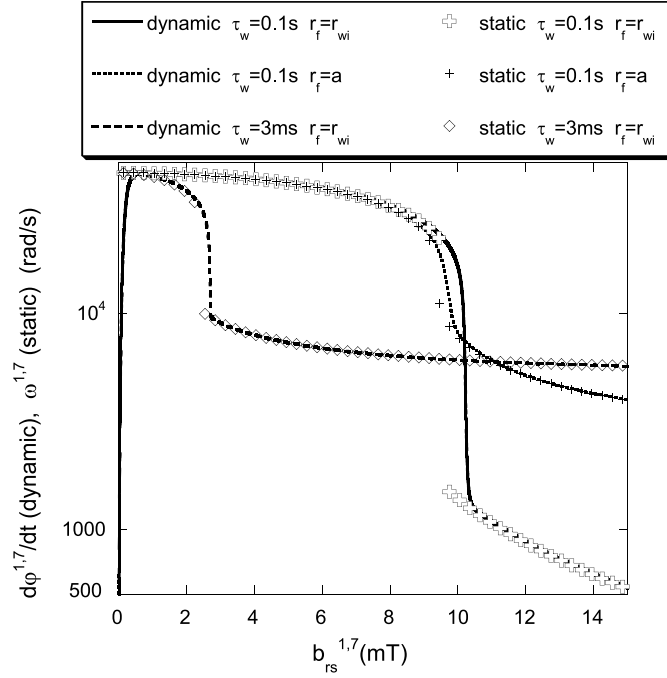
Figure 5. Frequency solution for the $m = 1, n = 7$ TM in the presence of feedback, obtained with both the dynamic and the stationary models. In the dynamic model b_{rs} ramps from 0 to 15 mT in 0.12 s. Three cases are considered: (1) $\tau_w = 0.1$ s, $r_f = r_{wi}$, $K_p = -10 \times 0.96 \times \pi/r_f$; (2) $\tau_w = 0.1$ s, $r_f = a$, $K_p = -2.25 \times 0.96 \times \pi/r_f$; (3) $\tau_w = 3$ ms, $r_f = r_{wi}$, $K_p = -2.4 \times 0.96 \times \pi/r_f$. In all these cases we take $K_d = \tau_c K_p$. Note the logarithmic scale in the y-axis.

and 10 show the final $\hat{b}_a^{m,n}$ and $|V_c^{m,n} \cdot I_c^{m,n}|/N_c$ computed by the dynamic model after 30 ms of simulation, performing a scan on the gains. An equilibrium is reached, since the condition $\mathrm{d}^2\varphi/\mathrm{d}t^2(\mathrm{d}\varphi/\mathrm{d}t)^{-1}\tau_V \ll 1$ is fulfilled at the end of the simulations. For a given K_d, the feedback performance improves by increasing K_p up to an optimum range of values, above which $\hat{b}_a^{m,n}$ is not reduced any more, while the coils power considerably increases. This property has already been pointed out in [8] and is verified in the RFX-mod experiment. The reason is that the feedback not only counteracts the edge TM amplitude, but also determines its equilibrium frequency as a consequence of the electromagnetic torque. When K_p exceeds the optimum range of values, the TM begins to rotate too fast, and the feedback, which is affected by the unavoidable delays τ_c, τ_d, cannot reduce the edge amplitude any more. The faster rotation, if not followed by a reduction of $\hat{b}_a^{m,n}$, requires higher power from the coils. A similar trend is seen for the derivative gain: the small amount of $K_d = \tau_c K_p$ which compensates the pole in the current transfer function (see equations (28), (31)), is beneficial both for $\hat{b}_a^{m,n}$ and for the efficiency, while any further increase risks raising significantly the power requested to the coils. We can say that the optimum choice (at least for $\tau_w = 0.1$ s) could be $K_d = \tau_c K_p$ with $-12 \times 0.96 \times \pi/r_{wi} < K_p < -10 \times 0.96 \times \pi/r_{wi}$. Note that in the case $K_d = 3\tau_c K_p$ two points of the K_p scan are not shown: for the case $K_p = -9 \times 0.96 \times \pi/r_{wi}$ the equilibrium condition is not fulfilled yet after 30 ms and some more time would be requested; instead, in the case $K_p = -8.25 \times 0.96 \times \pi/r_{wi}$ the solution of the dynamic model is unstable and never approaches the equilibrium condition. We have in fact verified that, raising K_p or K_d too much above the optimal range, the dynamic model could not reach the equilibrium condition
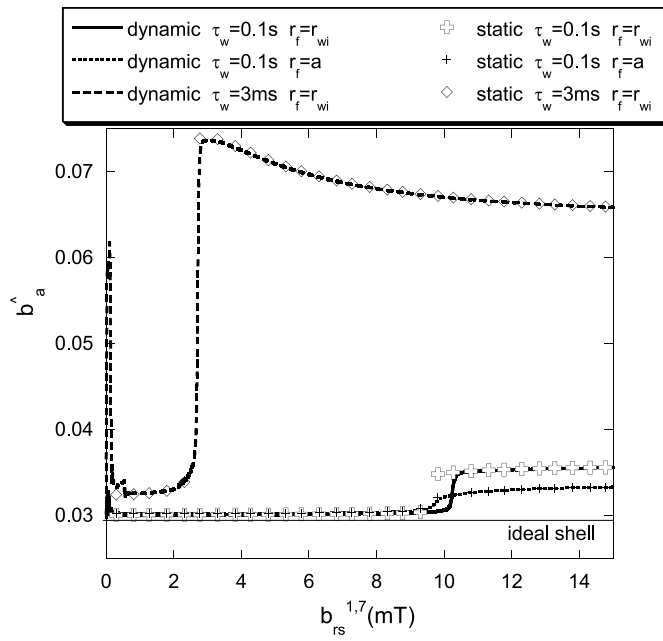
Figure 6. For the same solutions of figure 5 the ratio $\hat{b}_a^{m,n}$ is given. The straight line represents the value in the case of an ideal shell in place of the resistive shell.
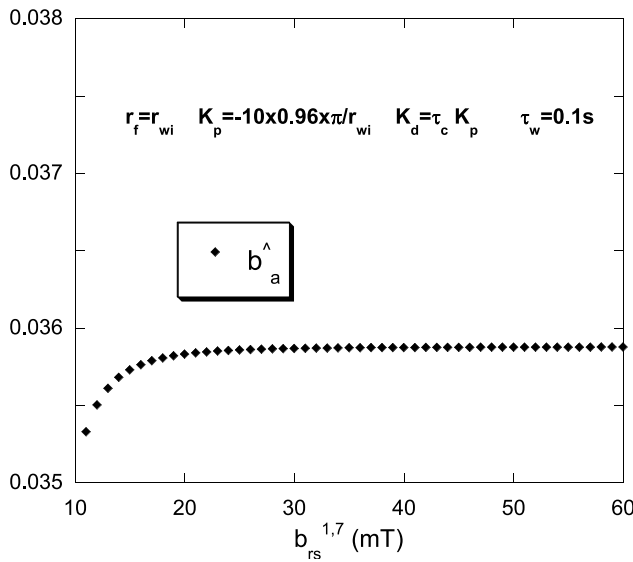

Figure 7. Computation of $\hat{b}_a^{m,n}$ for the $m = 1$, $n = 7$ TM with the stationary model. This plot extends the points reported in figure 6 for the first simulation in the low-frequency branch.

$\mathrm{d}^2\varphi/\mathrm{d}t^2(\mathrm{d}\varphi/\mathrm{d}t)^{-1}\tau_V \ll 1$, showing oscillations or divergent trends both in the frequency and $\hat{b}_a^{m,n}$. This behaviour may be related to the instability at high gains discussed in [21]. Nevertheless, we would stress that these instabilities occur for gain values away from the region of interest where the feedback has the optimum performance and efficiency. These

17
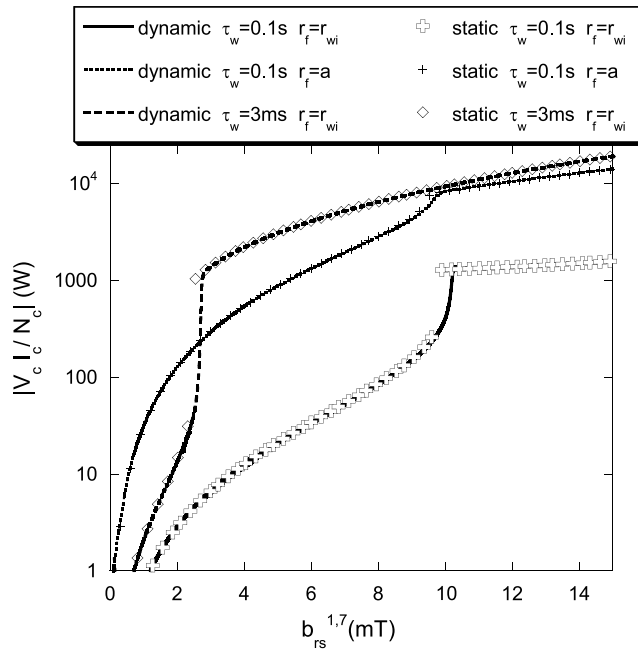
Figure 8. For the same solutions of figure 5 an estimate of the maximum power required for the coils.
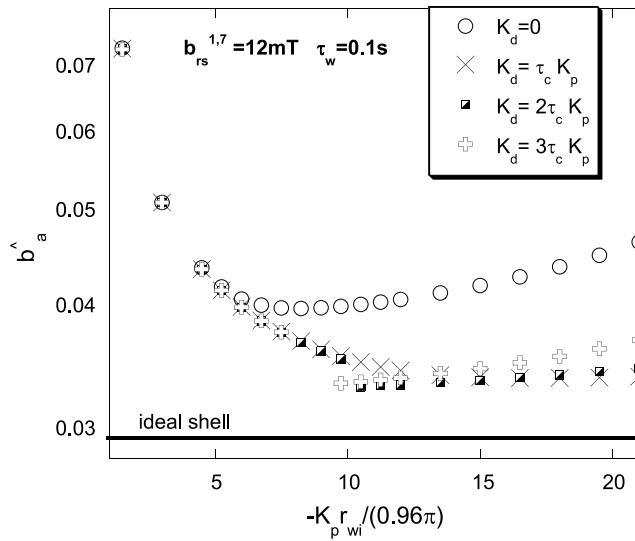

Figure 9. $\hat{b}_a^{m,n}$ for the $m = 1$ $n = 7$ TM obtained with the dynamic model after 30 ms computation. The straight line represents the value in the case of an ideal shell in place of the resistive shell. The control radius is $r_f = r_{wi}$. Note the logarithmic scale in the y-axis.

instabilities are not seen in the stationary model, which would predict equilibrium states for every value of the gains. Moreover, the stationary model can have multiple solutions for a given value of the gains, but only one of these equilibria can be reached by the dynamic model starting from the adopted initial conditions. For this reason the stationary model should be
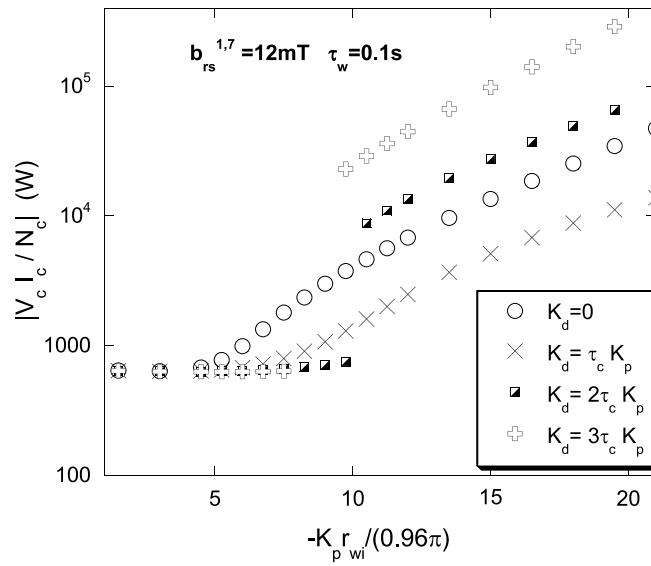
Figure 10. Estimate of the coils maximum power for the same scan of figure 9.
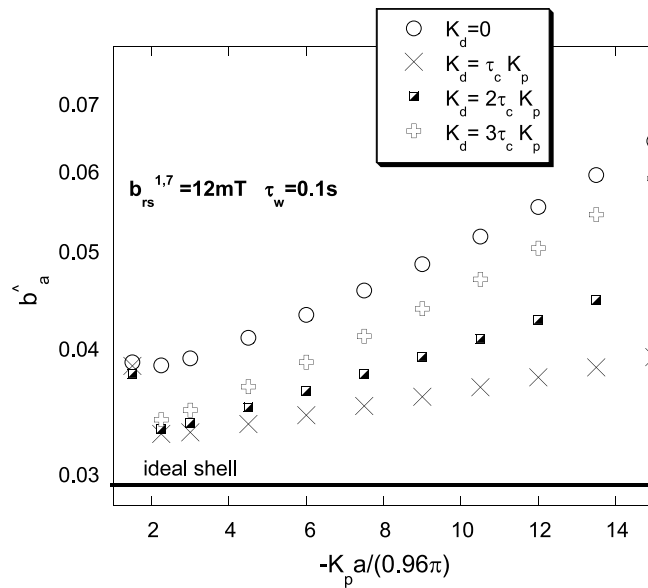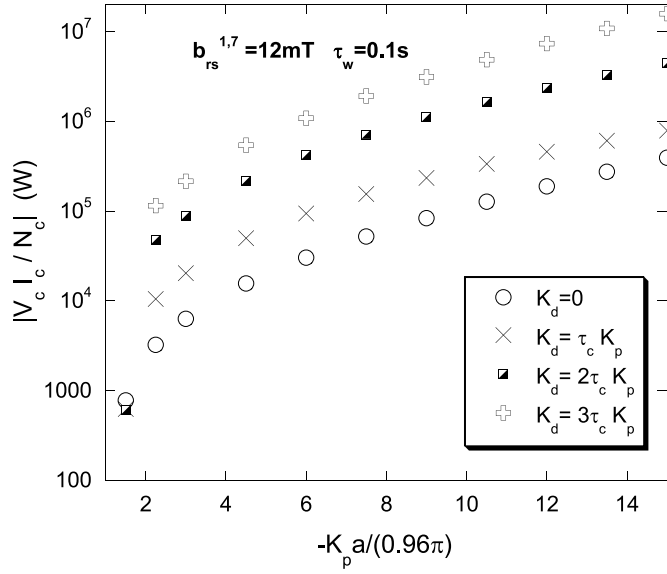

Figure 11. Same scan of figure 9, with the control radius at $r_f = a$. Note the logarithmic scale in the y-axis.

considered with some care, since it may indicate equilibrium states which are not reachable starting from physically meaningful initial conditions.

5.4. Gains dependence for the control radius at $r_f = a$

Figures 11 and 12 repeat the gain scan shown in figures 9 and 10 with the control radius at $r_f = a$. As anticipated in section 5.2, the values for $\hat{b}_a^{m,n}$ are not reduced while the coils power

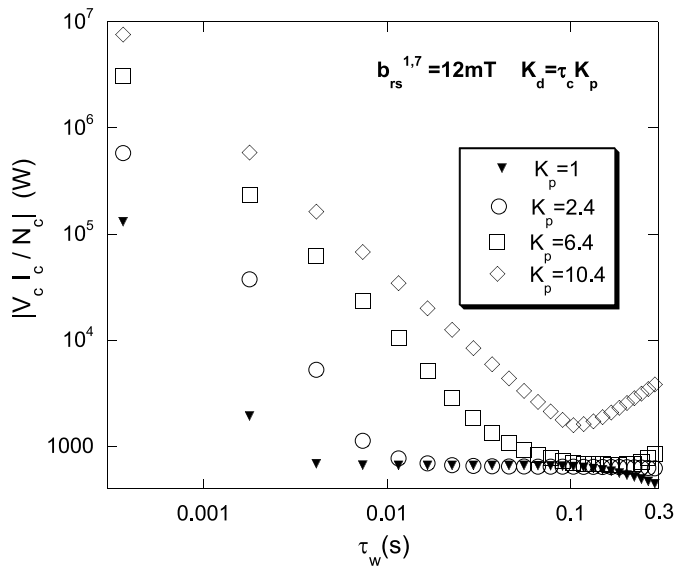**Figure 12.** Estimate of the coils maximum power for the same scan of figure 11.

increases with respect to the feedback at $r_f = r_{wi}$. Therefore, with a simple P.D. controller, the feedback cannot do better than what the shell does in the high frequency branch (or what an ideal shell does) even with the control radius at $r_f = a$: in figures 8 and 10 the $\hat{b}_a^{m,n}$ are all above the value that we would have with an ideal shell in place of the resistive shell. Consequently, the feedback counteracts a larger radial field moving the control radius from $r_f = r_{wi}$ to $r_f = a$, and the required power increases. The reason for the existence of a lower limit in $\hat{b}_a^{m,n}$ could be related to the non-linear character of the electromagnetic torque (7). In fact we have verified that, in principle, a feedback-linearization technique [23] could make $\hat{b}_a^{m,n}$ arbitrarily small. Feedback linearization means to cancel the non-linearity of the model equations by a suitable feedback law, which can be also much involved; so the system of equations in the presence of feedback becomes linear. The limit is that this technique is model dependent, and indeed we have verified it only in a much simpler configuration with a shell described by the thin-shell dispersion relation, and with $\tau_d = \tau_c = 0$ in relations (29) and (31). Its applicability in a realistic case, including equation (24) and all the delays introduced by the coils amplifiers and the measurements acquisition, is still to be investigated.

5.5. Shell time constant dependence

Under the assumptions discussed in section 5.1 for shell thickness and conductivity, figures 13 and 14 investigate the feedback efficiency dependence on τ_w, in the low-frequency branch. This analysis is not expected to give the optimum shell for the feedback, since all possible values of conductivity and thickness are not explored. Nevertheless, it highlights the fundamental trends. The imposed mode amplitude at the resonant surface is the same as in figures 9–12, and the control radius is set at $r_f = r_{wi}$. The τ_w scan is made for some K_p covering a large range of values, keeping $K_d = \tau_c K_p$. The points represent again the final values after 30 ms simulations with the dynamic model (the final equilibrium condition is fulfilled). For any K_p, both $\hat{b}_a^{m,n}$ and the coil power increase reducing τ_w too much. At the same time it is not necessary
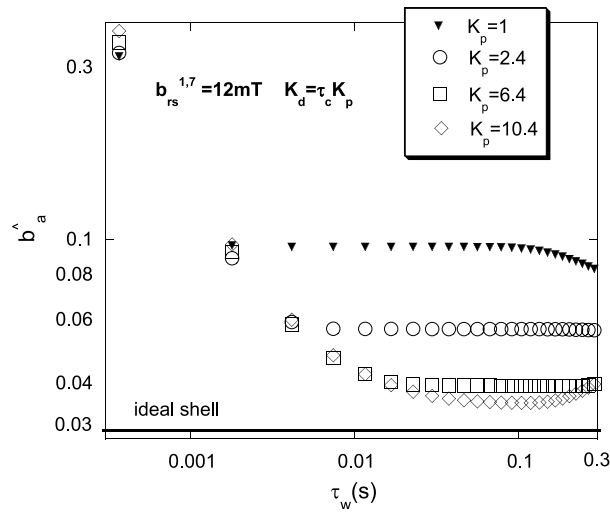
Figure 13. $\hat{b}_a^{m,n}$ for the $m = 1$ $n = 7$ TM obtained with the dynamic model after 30 ms computation; the K_p values are multiples of $-0.96\pi/r_{wi}$. The control radius is at $r_f = r_{wi}$. The straight line represents the value in the case of an ideal shell in place of the resistive shell. Note the logarithmic scale in both axes.

Figure 14. Estimate of the coils maximum power for the same scan of figure 13.

to have a very long time constant to ensure a good feedback: in fact, both $\hat{b}_a^{m,n}$ and the coil power show saturation, depending on K_p, with τ_w. An optimum range of values can be seen around $\tau_w \sim 100$ ms. Maybe these values are the best compromise between the requirements of having a shell that guarantees a good passive stabilization and, at the same time, does not hinder the feedback action. The analysis indicates that for too low τ_w the dominant effect is the poor shell passive stabilization. The trends of figures 13 and 14 are confirmed repeating the computation with a copper shell for every value of τ_w, that is decreasing the shell thickness

below 3 mm for $\tau_w < 100$ ms.

6. Multi-mode analysis

The previous single-mode analysis is important to point out the main aspects of the TMs feedback, but incomplete for an RFP, since the multi-mode non-linear interaction is a crucial element of the dynamic. In this section we are going to show some simulations performed with the dynamic model including the electromagnetic torque produced by the non-linear interaction between different TMs, represented by formula (8). Since in this case the run time of the simulations increases considerably, we are going to show a smaller number of examples with respect to the previous section. The results will confirm the previous single-mode analysis results.

6.1. Preliminary considerations

The RFP dynamo modes are the internally resonant $m = 1$ TMs, which in RFX-mod have $n \geqslant 7$. A secondary branch of $m = 0$ modes with a large n spectrum resonating at the reversal surface ($q = 0$) is important for the non-linear interaction with $m = 1$. In fact, in the non-linear component of the electromagnetic torque (8) we have triplets made by two $m = 1$ TMs with different n and one $m = 0$ mode. We do not consider triplets of $m = 0$ modes, because this kind of coupling, being a self-interaction between $m = 0$ modes, would give zero contribution in equation (20) to the total electromagnetic torque at the reversal surface integrated over the angular co-ordinates $\sum_{n>0} \delta T_{\mathrm{EM},\phi}^{0,n}$, and therefore to the flux-surface averaged angular velocity (the poloidal component of the torque is zero for $m = 0$ modes as seen in equation (21)). The superimposition of the $m = 0$ modes determines an island-like structure at the reversal surface, which is dragged by the local average toroidal velocity. This effect is described by the phase evolution equation (23) for $m = 0$ modes. However, the structure can also change toroidal shape due to the $m = 0$ self-interaction. This effect is not related to the modification of the average velocity at the reversal surface and cannot be described by the model considered here. Nevertheless, it should take into account in the phase evolution of the $m = 0$ modes. The problem has been discussed in [12], where it has been shown that the minimization in the sense of the L^2-norm of the electromagnetic torque angular function $\oint [T_{\mathrm{EM},\phi}^{m=0}(\phi)]^2 \, \mathrm{d}\phi$ produced by the $m = 0$ self-interaction in the vicinity of the reversal surface requires a specific phase-locking of $m = 0$ modes:

$$\varphi^{0,n} = n\phi_0 - \Delta_0; \qquad \Delta_0 = \pm \pi/2. \tag{45}$$

Here ϕ_0 and Δ_0 determine, respectively, the toroidal location and the shape of the island-like $m = 0$ structure. The minimization of the electromagnetic torque is a plausible condition that facilitates the balance with the other terms, such as inertia and viscosity, in the equation of motion. A statistical analysis carried out on the RFX data has shown the preference for the value $\Delta_0 = \pi/2$ [12]. A similar analysis has not been done in RFX-mod as yet, but the observations confirm that the $m = 0$ locking is not changed. We take into account the $m = 0$ self-interaction imposing the phase-locking relation (45) with $\Delta_0 = \pi/2$ as initial condition in equations (23) for $\varphi^{0,n}$. In this case, relation (45) will be maintained during the evolution with a time dependent ϕ_0 dragged by the average fluid velocity at the reversal surface: $\mathrm{d}\phi_0/\mathrm{d}t = \sum_{j=1,j_{\max}} g_j(t)\, u_j(r_{0,1})$. The assumption that the $m = 0$ modes remain always phase-locked according to (45) is not exactly verified in the experimental case, but at the moment we do not have a better model for the $m = 0$ phase evolution. At $t = 0$ the values of ϕ_0 and $\varphi^{1,n}$ are set at random. We will show some examples considering the evolution of
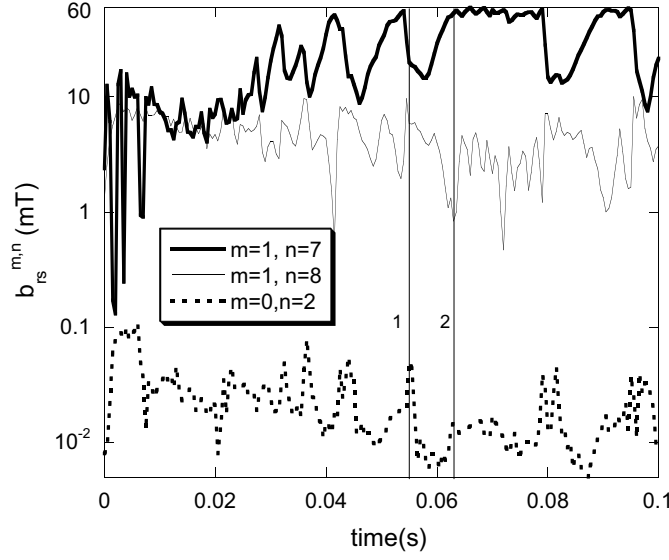
Figure 15. Example of the mode amplitude at the resonant surface estimated on the shot 23810. They are imposed in the multi-mode simulations with a factor $[1 - \exp(-2000 \times t)]$ to ensure the vanishing initial condition. Note the logarithmic scale in the y-axis.

the modes $m = 1$, $n = 7$–19 non-linearly interacting with the modes $m = 0$, $n = 1$–12. The amplitudes at the resonant surfaces $\Psi_{s0}^{m,n}(t)$ are imposed according to the values estimated from the edge magnetic data using a Newcomb's equation solver [16] for the adopted RFX-mod reference shot. Since we are considering a passive boundary different from the RFX-mod one, these amplitudes must be taken only to be indicative of a high current RFP regime. In figure 15 they are shown for three modes. The $m = 1$, $n = 7$, which is much larger than the others, is called the dominant mode. The other modes are called the secondary modes. Note that the $m = 0$ amplitude is very low. This is an example of the quasi-single-helicity state (QSH), which RFX-mod exhibits in the high plasma current regime [9, 22]. A sawtoothing behaviour, with an energy transfer between the dominant and the secondary modes, is also seen: when the dominant modes goes down, the secondary have a sudden increase (vertical line 1) and vice versa (vertical line 2). The feedback performance will be characterized not only by the ratios $\hat{b}_a^{m,n}$ but also by the global geometrical distortion of the plasma surface due to the TMs overlapping. This is a standard method used in the RFX-mod data analysis: the plasma surface displacement ξ_a is obtained from the measured radial field at $r = a$ using the linear ideal-MHD Faraday–Ohm's law

$$b_r(a, \theta, \phi) = \boldsymbol{B}_0(a) \cdot \nabla \xi_a(\theta, \phi) \rightarrow \xi_a^{m,n} = -\mathrm{i} r b_r^{m,n}(a)/(m B_0^\theta(a) - n\varepsilon(a) B_0^\phi(a)). \tag{46}$$

While $\hat{b}_a^{m,n}$ represents the edge radial field normalized to the mode amplitude at the resonant surface, therefore the eigenfunction shape, the displacement ξ_a is a sort of normalization of the edge radial field with the equilibrium field. The plasma surface displacement is divided into the contributions produced by all the $m = 0$ and by all the $m = 1$ modes separately: the $m = 0$ modes determine a sausage deformation $\xi_0(\phi)$ of the plasma surface, while the $m = 1$ are associated with a helical shift $\xi_1(\phi)$ with poloidal phase $\Theta(\phi)$:

$$\xi_a(\theta, \phi) = \xi_0(\phi) + \xi_1(\phi) \cos[\theta - \Theta(\phi)]. \tag{47}$$

23

The quantities $\xi_0(\phi)$, $\xi_1(\phi)$, $\Theta(\phi)$ can be easily derived from the displacement harmonics $\xi_a^{0,n}$, $\xi_a^{1,n}$. We also determine the power $P_{i,j}$ required by each coil, combining the current and voltage discrete Fourier harmonics $V_c^{m,n}$, $I_c^{m,n}$ computed by the model:

$$P_{i,j} = \frac{I_{i,j}}{N_c} V_{i,j}; \qquad i = 1, \ldots, M; \ j = 1, \ldots, N,$$

$$I_{i,j} = \sum_{m,n} I_c^{m,n} e^{i(m\theta_i - n\phi_j)}; \qquad V_{i,j} = \sum_{m,n} V_c^{m,n} e^{i(m\theta_i - n\phi_j)}. \tag{48}$$

The coils are supposed to be centred at the angles $\theta_i = 2\pi/M \times (i-1)$, $i = 1, \ldots, M = 4$, $\phi_j = 2\pi/N \times (j-1)$, $j = 1, \ldots, N = 48$.

6.2. Simulation examples

Four simulations have been performed keeping the shell at $r_{wi} = 0.475$ m, as in the single-mode analysis, the control radius at $r_f = r_{wi}$ and varying only the shell time constant: $\tau_w = 0.1$ s (s.1), $\tau_w = 0.01$ s (s.2), $\tau_w = 0.003$ s (s.3), $\tau_w = 0.2$ s (s.4). Three extra simulations are performed with $\tau_w = 0.1$ s:

> (s.5): same gains of (s.1) and $r_f = r_{wi}$, but the shell at $r_{wi} = 0.5125$ m, corresponding to the position of the $\tau_w = 0.1$ s shell in RFX-mod;
> (s.6): $r_{wi} = 0.475$ m without feedback;
> (s.7): $r_{wi} = 0.475$ m and moving the control radius at the plasma edge $r_f = a$.

All the simulations apart from the (s.6), which is performed for 30 ms, are carried out for 100 ms. The derivative gains are fixed by the condition $K_d^{m,n} = \tau_c K_p^{m,n}$ for each mode. The values for the proportional gains are imposed performing a preliminary scan with the stationary single-mode model: for each mode the largest gain compatible with the condition $|V_c^{m,n} I_c^{m,n}|/N_c < 2500$ W at the high–low frequency transition $b_{rs} = b_{h-l}$, just to fix a power limit, is imposed. They have a decreasing trend with the toroidal mode number n. The no-feedback simulation (s.6) shows a sudden wall-locking of all TMs. The single-mode b_{h-l} thresholds are exceeded only by few of them, but, as already pointed out in [10], the non-linear interaction between the different TMs significantly reduces the effective thresholds. Figure 16(b) plots the $m = 0$ plasma surface distortion $\xi_0(\phi)$ produced by the phase-locking (45). Note that the structure is stationary due to the wall-locking. In figure 16(a) the $m = 1$ plasma surface distortion $\xi_1(\phi)$ is plotted: the $m = 1$ modes, starting from random phases, not only wall-lock but also phase-lock together according to $\varphi^{1,n} \approx n\phi_0 - \Delta_1$ and produce a toroidally localized structure close to the angle ϕ_0. This is a well-known phenomenon observed in the experiment and already explained in [12]. For the $m = 1$ phase-locking, Δ_1 is a free parameter [12]. The $m = 1$ phase-locking relation is satisfied only approximately due to the irregular time behaviour of the mode amplitudes at the resonant surfaces and the fact that the $m = 1$, $n = 7$ has an amplitude much larger than the other modes. The plots also indicate that the perturbation penetrates the shell, increasing in time. This effect will be quantified in figure 23. The final toroidal and poloidal velocity profiles, plotted in figure 17, are compatible, at least with the order of magnitude and the directions, with the RFX estimates relative to the intermediate/external region of the plasma, mentioned in section 5.1: we are comparing our result with the low density region of figure 8 published in [20], which considers the data in the presence of wall-locked and phase-locked TMs (the negative poloidal direction of that figure corresponds to our positive direction). As anticipated in section 5.1, this means that the choice of the unperturbed velocity profiles is sensible, since the final velocity profiles depend mainly on that choice. As a confirmation of the single-mode analysis, the feedback keeps the
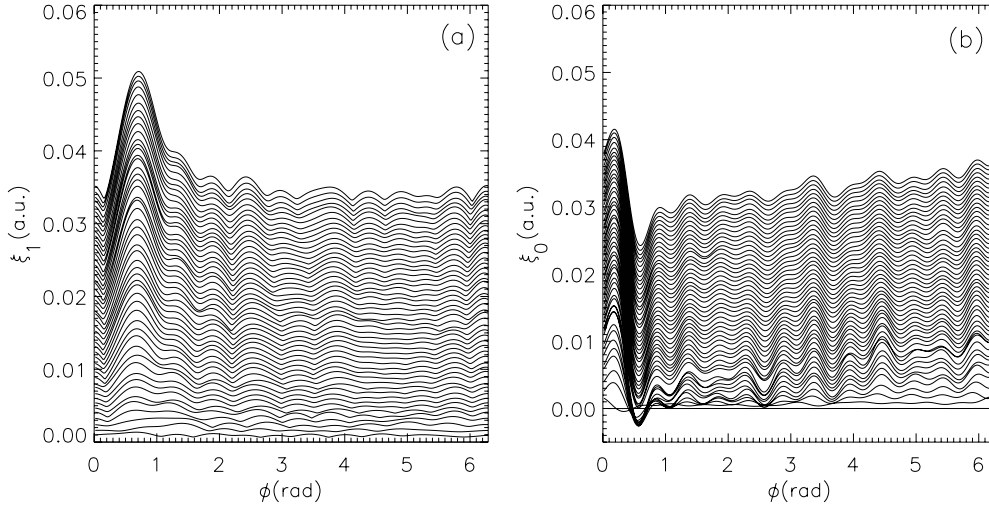
Figure 16. Plasma surface distortions $\xi_1(\phi)$ (*a*) and $\xi_0(\phi)$ (*b*) for the case with no-feedback (s.6). The simulation is carried out for 30 ms. The curves, which represent different times, are superimposed with an offset.

TMs into rotation in the multi-mode simulations also. This is shown in figure 18, considering the simulation (s.1). Due to the time-dependent amplitudes at the resonant surfaces and the non-linear interaction between the different TMs, the uniform rotations seen in the single-mode analysis are recovered only at irregular intervals. Moreover, the values of the rotation frequencies can also be different from those obtained in the single-mode analysis, since the non-linear interaction tends to maintain the TMs phase-locked together. This tendency is shown in figure 19, considering again the simulation (s.1): the phase-locking for the $m = 0$ is imposed, while the phase-locking for the $m = 1$ is a result of the simulation. The tendencies to rotate in the presence of feedback and to stay phase-locked together are both realized by the time derivative of the phase-locking relations for the $m = 0$ and $m = 1$ TMs:

$$\mathrm{d}\varphi^{0,n}/\mathrm{d}t = n\,\mathrm{d}\phi_0/\mathrm{d}t; \qquad \mathrm{d}\varphi^{1,n}/\mathrm{d}t \approx n\,\mathrm{d}\phi_0/\mathrm{d}t - \mathrm{d}\Delta_1/\mathrm{d}t. \qquad (49)$$

According to (49) the $m = 1$, $m = 0$ structures rotate close to each other, while the individual TMs have a differential rotation frequency. For $m = 1$ modes in particular, if a $\bar{n}$ such that $\bar{n}\mathrm{d}\phi_0/\mathrm{d}t \approx \mathrm{d}\Delta_1/\mathrm{d}t$ exists, a change in the rotation direction occurs for $n > \bar{n}$: this is evident in the first 40 ms of figure 18. The final velocity profile obtained in the simulation (s.1) at $t = 0.1$ s is similar to that shown in figure 17 in the absence of feedback, since all the mode frequencies are smaller than the unperturbed frequencies at that time. Note, however, that in figure 18 some modes accelerate close to the high frequency branch values at $t \approx 85$–90 ms. Figures 20 and 21 compare the ratios $\hat{b}_a^{m,n}$, time-averaged in the simulations (s.1)–(s.4), with the predictions of the stationary single-mode model obtained with gains similar to those of the simulations. Note a very good agreement between the simulations and the stationary single-mode computation: this means that, while the non-linear interaction between the different TMs affects their rotation frequencies, the ratios $\hat{b}_a^{m,n}$ depend mainly on the shell characteristics (assuming that the gains are in the optimum range). In the multi-mode simulations the fundamental results obtained in the single-mode analysis are recovered: the feedback prevents the shell penetration and fixes $\hat{b}_a^{m,n}$ at values close to the ideal shell ones. The performances are better increasing τ_w, but at the end a saturation is found since the two cases $\tau_w = 0.1$ s and $\tau_w = 0.2$ s are equivalent. Figure 21 shows a poor efficiency of the feedback in the control of the low n, $m = 0$ modes:
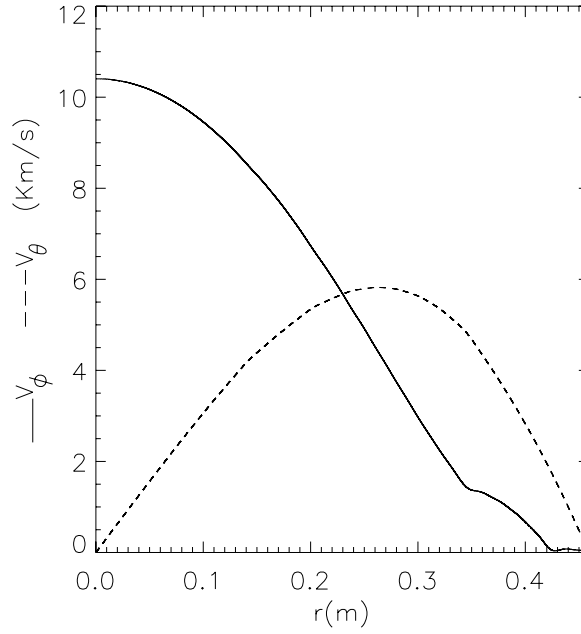
Figure 17. Toroidal $V_\phi(r) = R_0\Omega_\phi$ and poloidal $V_\theta(r) = r\Omega_\theta$ velocity profiles at the end of the no-feedback simulation (s.6).

this is simply due to the difficulty in producing these harmonics for such an active coils grid, a problem encountered in RFX-mod also. As already demonstrated in the single-mode analysis, for a given shell the ratios $\hat{b}_a^{m,n}$ do not depend on the control radius: this is confirmed in figure 22 comparing the simulations (s.1) and (s.7), which exhibit the same performances. On the other hand, the quantities $\hat{b}_a^{m,n}$ depend on the plasma shell distance, as demonstrated in the same figure by comparing the simulations (s.1) and (s.5). This is an obvious consequence of the fact that the feedback fixes $\hat{b}_a^{m,n}$ just above the ideal-shell values. Figure 23 demonstrates the same features of figure 22, by considering the maximum of the plasma surface distortion due to the $m = 1$ TMs as a function of time: this quantity is reduced by moving the shell to the plasma, rather than moving the control radius from $r_f = r_{wi}$ to $r_f = a$. The result of the no-feedback simulation (s.6) and the experimental estimate of RFX-mod (red curve) on the reference shot are also shown. In the (s.6) case the plasma surface distortion does not settle to a controlled value, as in the feedback case, but increases in time indicating the shell penetration. The quite good agreement between the simulation (s.5) and the RFX-mod curve should indicate that in the case of a multiple shell front end (as that of RFX-mod) it is mainly the longer time constant shell (the $\tau_w = 0.1$ s at $r_{wi} = 0.5125$ m) that determines the feedback performances. Figure 24 considers the maximum coil power $\max_{i,j}[P_{i,j}]$ as a function of time for all the feedback simulations performed with $r_{wi} = 0.475$ m. The plotted signals are smoothed to clarify the comparison between the different simulations. The curves confirm the single-mode analysis: reducing too much the shell time constant, or moving the control radius from $r_f = r_{wi}$ to $r_f = a$, increases the coil power requested by the feedback; a saturation with τ_w occurs, since the two cases $\tau_w = 0.1$ s and $\tau_w = 0.2$ s are equivalent. In conclusion, the TMs non-linear interaction is not seen to change the feedback performance and efficiency dependence on the shell time constant and on the control radius, which has been obtained in the single-mode analysis.

26
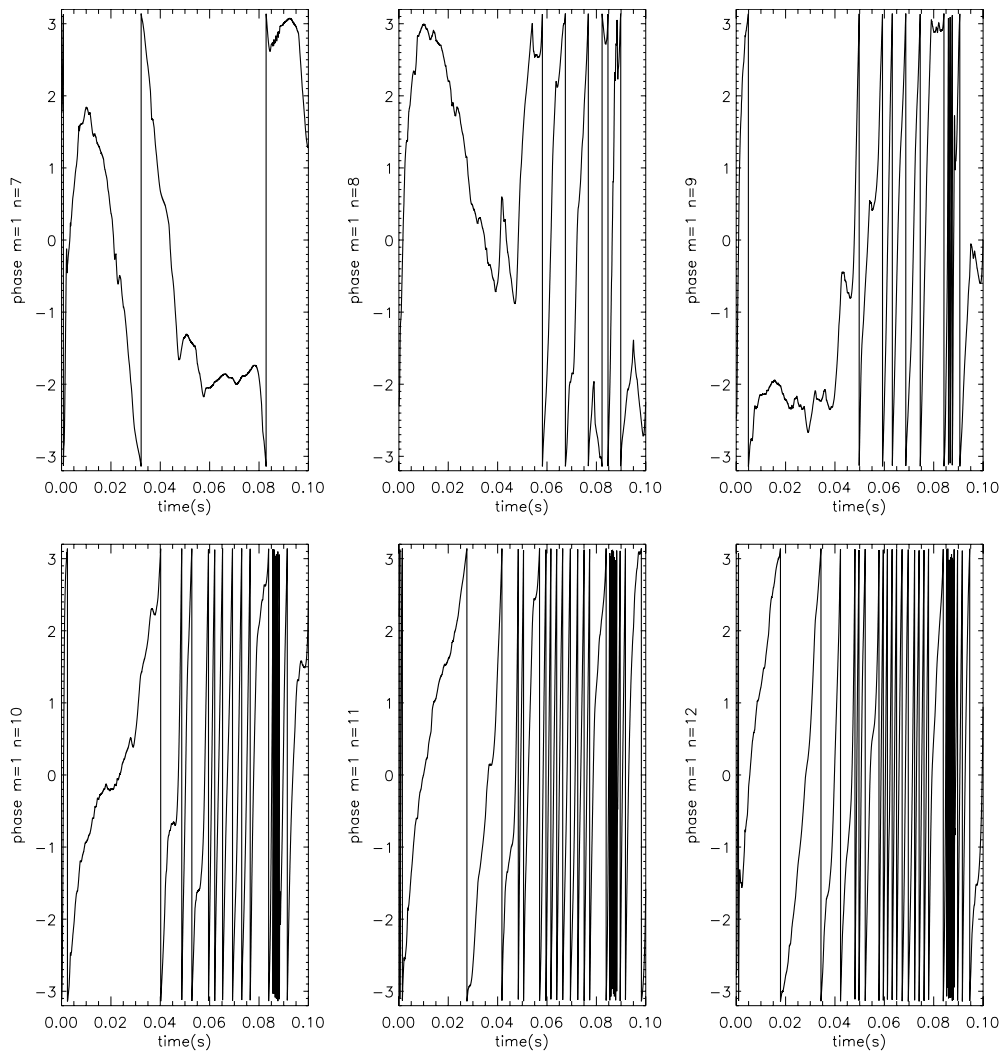
Figure 18. Phase (in radians) evolution of some $m = 1$ modes for the simulation (s.1): $\tau_w = 0.1\,\mathrm{s}$, $r_f = r_{wi} = 0.475\,\mathrm{m}$.

7. Concluding remarks

A study of the feedback on the RFP dynamo TMs, in a cylindrical force-free plasma surrounded by a single resistive shell with active coils placed outside it, has been performed. The adopted model solves the fluid momentum equation, the shell diffusion equation and the active coil power supply equation in closed-loop configuration. The CMC scheme [8, 9], in which the feedback variables are the TMs Fourier harmonics, has been implemented. The unavoidable delays related to the coils amplifiers, the feedback acquisition and real-time operations have been included. The coils delay can be compensated by a suitable derivative gain. However, very small values for these delays have been given in the computations. The feedback is shown to make the resistive shell behave like an ideal shell virtually for any value of TMs amplitudes
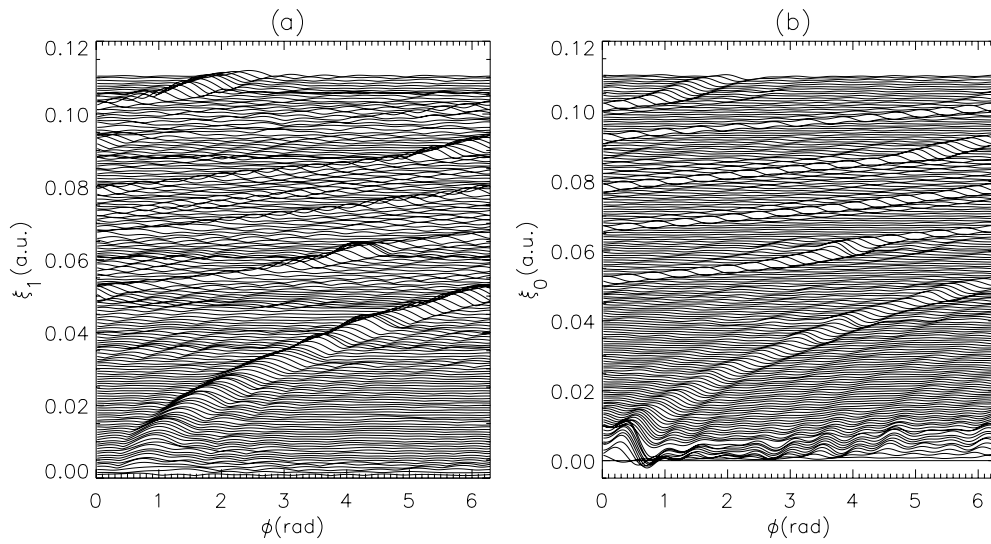
Figure 19. Plasma surface distortions $\xi_1(\phi)$ (*a*) and $\xi_0(\phi)$ (*b*) for the feedback case (s.1). The simulation is carried out for 100 ms. The curves, which represent different times, are superimposed with an offset.
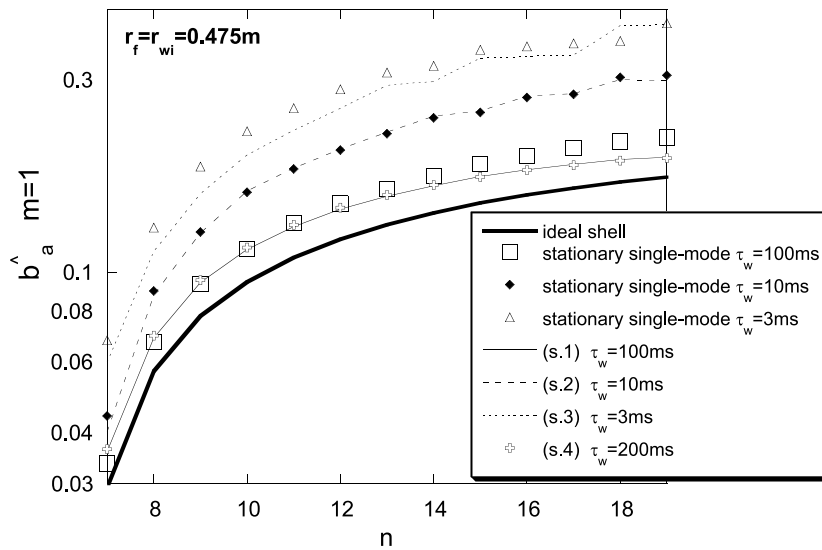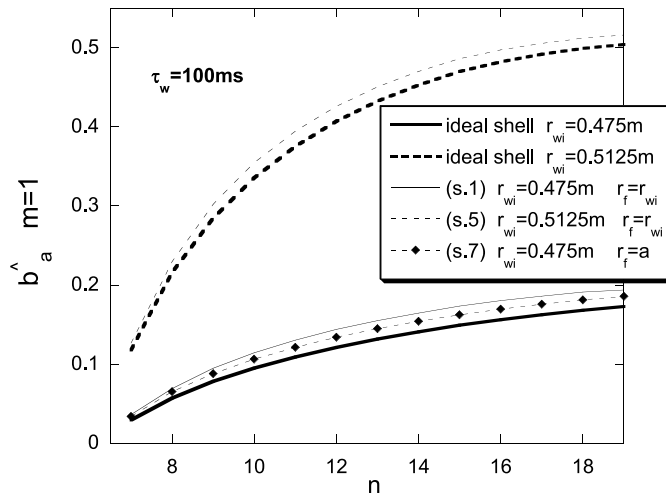

Figure 20. Time-averaged $\hat{b}_a^{m,n}$ for the various $m = 1$ TMs, obtained in the simulations (s.1)–(s.4). The predictions of the stationary single-mode model for gains similar to those of the simulations are also shown. The solid curve represents the values in the case of an ideal shell in place of a resistive shell. Note the logarithmic scale in the *y*-axis.

at the resonant surfaces. The transition from the high frequency rotation branch, related to the unperturbed fluid motion, to a slower frequency branch is not a problem any more: in fact, due to the feedback, TMs rotations never stop and the edge amplitudes remain close to the values they would have with an ideal shell in place of the resistive shell. For constant amplitude at the resonant surface, the feedback determines an equilibrium condition with uniform TM rotation.
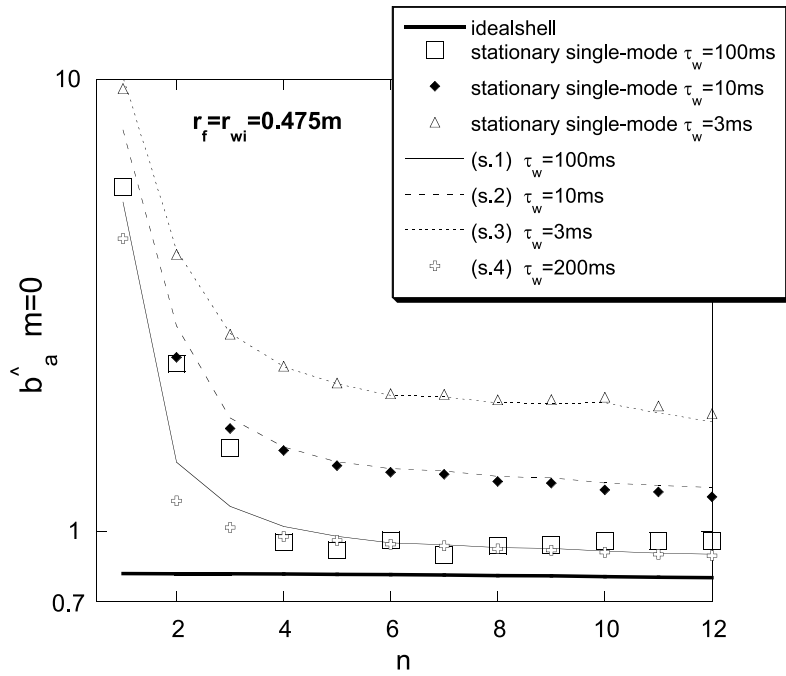
Figure 21. Time-averaged $\hat{b}_a^{m,n}$ for the various $m = 0$ TMs, obtained in the same simulations (s.1)–(s.4) of figure 20. The predictions of the stationary single-mode model for gains similar to those of the simulations are also shown. The solid curve represents the values in the case of an ideal shell in place of the resistive shell. Note the logarithmic scale in the y-axis.


Figure 22. Time-averaged $\hat{b}_a^{m,n}$ for the various $m = 1$ TMs, obtained in the simulations (s.1), (s.5), (s.7). In this case we keep fixed the shell time constant at $\tau_w = 0.1$ s. With respect to (s.1), in (s.5) the shell radius is moved farther from the plasma, and in (s.7) the control radius is moved at the plasma edge. The solid curves represent the values in the case of an ideal shell in the place of the resistive shell.
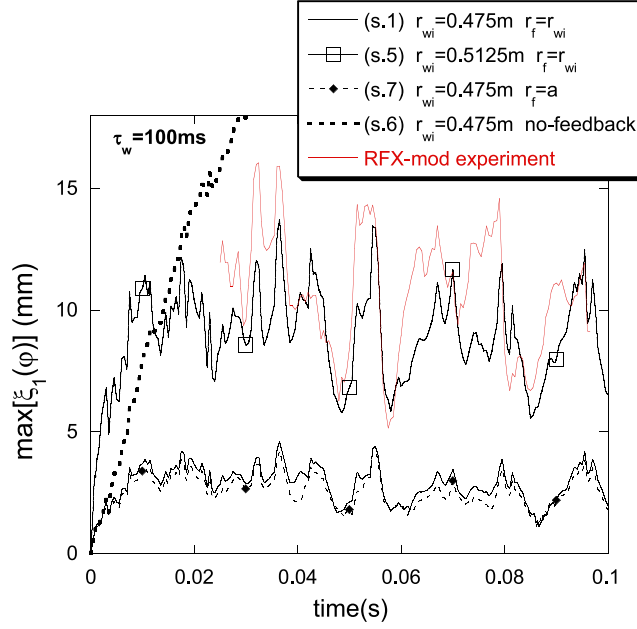
Figure 23. Maximum of the $m = 1$ plasma surface distortion as a function of time for the same simulations (s.1), (s.5), (s.7) of figure 22, and for the no-feedback simulation (s.6). The red curve is the value estimated in RFX-mod on the reference shot 23810: only the times greater than 30 ms, when the experimental equilibrium settles to the stationary value used in the simulations, are shown.

According to our model, feedback induced instabilities can occur only for gains too large and do not prevent the existence of a wide region of gain values in which the feedback performances are good. We have shown that good feedback performance and efficiency are obtained if τ_w is not too small. Moreover a saturation is seen with a copper shell for $\tau_w > 0.1$ s. A similar saturation is seen in the wall-locking threshold for the pure passive shell stabilization, as shown in figure 4. The explored τ_w range is limited by the condition $\delta_w \ll r_{wi}$ where equation (24) is valid. Nevertheless, this analysis indicates that a thick shell with a very large τ_w is not necessary and that the RFP can work with a relatively thin shell ($\tau_w \sim 100$ ms) aided by the feedback coils. The feedback beneficial effects on the dynamo TMs are currently observed in RFX-mod, where the highest plasma current ever reached in an RFP, 1.6 MA in the latest experimental campaign (shot 24533), has been obtained. The basic aspect of the CMC scheme, namely, the fact that the feedback variables are not the raw measurements, which unavoidably present the content of sideband harmonics produced by the coils grid, but the Fourier harmonic of the TMs, has been proven decisive to obtain the rotation stop avoidance in the experiment. With a P.D. controller, the feedback cannot reduce the ratios $\hat{b}_a^{m,n}$, between the amplitudes at the plasma edge $r = a$ and at the resonant surface, below the values obtained with an ideal shell in the place of the resistive shell, even with the control radius at $r_f = a$. We believe that this is related to the non-linear character of the model describing the TMs dynamic in the presence of feedback. If a more sophisticated controller were not feasible, we were obliged to rely on the standard P.D., the conclusion would be that the shell should be placed as close as possible to the plasma, in order to minimize $\hat{b}_a^{m,n}$. At present, the main limitation of the RFX-mod feedback is the quite large plasma–shell distance (5.35 cm): our analysis indicates that reducing it would be beneficial for the edge radial field control.
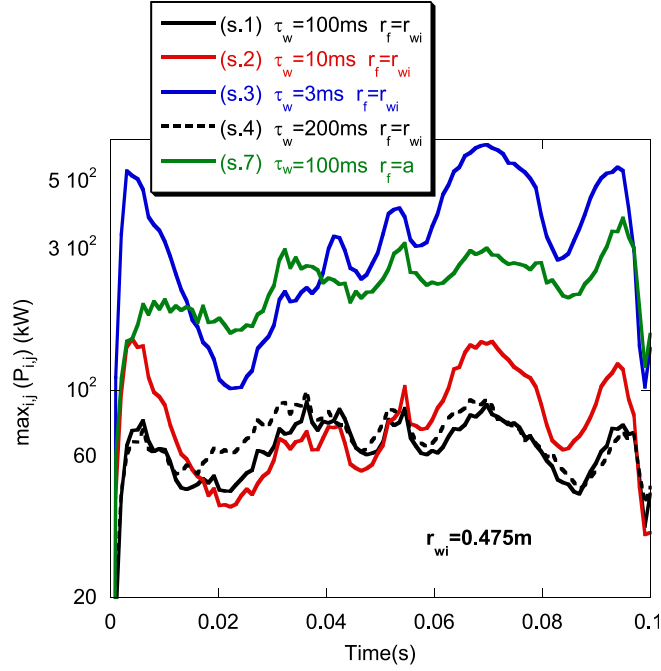
Figure 24. Maximum of the coil power as a function of time for the simulations with $r_{wi} = 0.475$ m. The signals are smoothed for clarity reason. Note the logarithmic scale in the y-axis.

Appendix A. Newcomb's equation and electromagnetic torque

In this section we present the formulae for the electromagnetic torque produced by the non-linear interaction between TMs, which have been obtained in [14]. Here the expressions are slightly generalized in order to take into account the non-ideal boundary conditions. The starting point is Newcomb's equation, which describes the TMs radial profiles inside the plasma.

Appendix A.1. Newcomb's equation

Within the cylindrical force-free approximation, the RFP equilibrium is given by

$$\nabla \times \boldsymbol{B}_0 = \mu_0 \boldsymbol{J}_0 = \sigma(r)\boldsymbol{B}_0; \qquad \boldsymbol{B}_0(r) = (0, B_{0\theta}(r), B_{0\phi}(r)). \qquad (A.1)$$

For the numerical computations the standard representation $\sigma(r) = (2\theta_0/a)(1 - (r/a)^\alpha)$ is adopted [24].

The TMs radial profiles are obtained from the ideal-MHD force balance equation:

$$\nabla \times (\boldsymbol{J} \times \boldsymbol{B}) = 0 \Rightarrow (\boldsymbol{B} \cdot \nabla) \boldsymbol{J} - (\boldsymbol{J} \cdot \nabla)\boldsymbol{B} = 0. \qquad (A.2)$$

Separating the linear from the non-linear terms in the perturbations as done in [14], we get

$$(\boldsymbol{j} \cdot \nabla)\boldsymbol{B}_0 + (\boldsymbol{J}_0 \cdot \nabla)\boldsymbol{b} - (\boldsymbol{b} \cdot \nabla)\boldsymbol{J}_0 - (\boldsymbol{B}_0 \cdot \nabla)\boldsymbol{j} = \frac{\boldsymbol{A}}{\mu_0}, \tag{A.3}$$

$$\frac{\boldsymbol{A}}{\mu_0} = (\boldsymbol{b} \cdot \nabla)\boldsymbol{j} - (\boldsymbol{j} \cdot \nabla)\boldsymbol{b}. \tag{A.4}$$

These equations must be coupled with

$$\nabla \cdot \boldsymbol{b} = 0, \tag{A.5}$$

$$\nabla \times \boldsymbol{b} = \mu_0 \boldsymbol{j}. \tag{A.6}$$

From (A.1), (A.3)–(A.6) and definition (1) we get

$$b_\theta^{m,n} = -\frac{m}{H^{m,n}}\frac{\partial \psi^{m,n}}{\partial r} + \frac{n\varepsilon\sigma}{H^{m,n}}\psi^{m,n} + \frac{n\varepsilon r^2}{H^{m,n}F^{m,n}}A_r^{m,n}, \tag{A.7}$$

$$b_\phi^{m,n} = \frac{n\varepsilon}{H^{m,n}}\frac{\partial \psi^{m,n}}{\partial r} + \frac{m\sigma}{H^{m,n}}\psi^{m,n} + \frac{mr^2}{H^{m,n}F^{m,n}}A_r^{m,n}, \tag{A.8}$$

$$\mu_0 j_r^{m,n} = \sigma b_r^{m,n} + i\frac{r}{F^{m,n}}A_r^{m,n}, \tag{A.9}$$

$$\mu_0 j_\theta^{m,n} = \sigma b_\theta^{m,n} + i\frac{rB_{\theta 0}}{F^{m,n}}\frac{d\sigma}{dr}b_r^{m,n} + i\frac{r}{F^{m,n}}A_\theta^{m,n} + \frac{r^2(\sigma B_{\phi 0} - 2B_{\theta 0}/r)}{(F^{m,n})^2}A_r^{m,n}, \tag{A.10}$$

$$\mu_0 j_\phi^{m,n} = \sigma b_\phi^{m,n} + i\frac{rB_{\phi 0}}{F^{m,n}}\frac{d\sigma}{dr}b_r^{m,n} + i\frac{r}{F^{m,n}}A_\phi^{m,n} - \frac{r^2\sigma B_{\theta 0}}{(F^{m,n})^2}A_r^{m,n} \tag{A.11}$$

and a second-order ordinary differential equation for the function ψ:

$$\frac{\partial}{\partial r}\left[f^{m,n}\frac{\partial}{\partial r}\psi^{m,n}\right] - g^{m,n}\psi^{m,n} = \frac{V^{m,n}}{n\varepsilon}. \tag{A.12}$$

Here we have defined

$$\varepsilon(r) = r/R_0; \qquad H^{m,n}(r) = m^2 + n^2\varepsilon^2; \qquad f^{m,n}(r) = r/H^{m,n}, \tag{A.13}$$

$$F^{m,n}(r) = mB_{\theta 0} - n\varepsilon B_{\phi 0}; \qquad G^{m,n}(r) = mB_{\phi 0} + n\varepsilon B_{\theta 0}, \tag{A.14}$$

$$g^{m,n}(r) = \frac{1}{r} + \frac{rG^{m,n}}{H^{m,n}F^{m,n}}\frac{d\sigma}{dr} + \frac{2mn\varepsilon\sigma}{(H^{m,n})^2} - \frac{r\sigma^2}{H^{m,n}}, \tag{A.15}$$

$$V^{m,n}(r) = -i\frac{r^2}{F^{m,n}}A_\theta^{m,n} + \frac{2r^2 B_{\theta 0}}{(F^{m,n})^2}A_r^{m,n} - \frac{mr^3\sigma G^{m,n}}{H^{m,n}(F^{m,n})^2}A_r^{m,n} - r\frac{\partial}{\partial r}\left[\frac{mr^2 A_r^{m,n}}{H^{m,n}F^{m,n}}\right]. \tag{A.16}$$

A perturbative approach is adopted: in equations (A.7)–(A.12) and (A.16) the non-linear terms $\boldsymbol{A}$ act as source terms, since they are intended to be evaluated using the solutions of equation (A.12) in the linear approximation. This is the so-called *Newcomb's equation*:

$$\frac{\partial}{\partial r}\left[f^{m,n}\frac{\partial}{\partial r}\psi^{m,n}\right] - g^{m,n}\psi^{m,n} = 0. \tag{A.17}$$

For the linear solutions, expressions (A.7)–(A.11) hold letting $\boldsymbol{A} = 0$. Note that all these expressions are derived in the framework of ideal-MHD, and they are not valid in the proximity

of the mode resonant surfaces $r_{m,n}$, where $F^{m,n}(r_{m,n}) = 0$. In the proximity of the mode resonant surface the linear solution (A.17) behaves like

$$\psi^{m,n}(x) = \Psi_s^{m,n} + \lambda^{m,n} x(\ln|x| - 1) + p^{m,n} x + \cdots, \qquad x = \frac{r - r_{m,n}}{r_{m,n}}. \tag{A.18}$$

The coefficient $p^{m,n}$ can be discontinuous across the resonant surface. This is related to the derivative discontinuity introduced in formula (3). Definition (A.4), and relations (A.7)–(A.11) in the linear approximation, brings to the following expressions for A in terms of the linear solutions:

$$A^{m,n} = \sum_{\substack{m_1, n_1, m_2, n_2 \,\in\, \mathbb{Z} \\ (m_1, n_1) + (m_2, n_2) = (m, n)}} A^{m,n}_{m_1, n_1, m_2, n_2}, \tag{A.19}$$

where for a triplet of modes such that $(m_1, n_1) + (m_2, n_2) = (m, n)$ we have

$$(A^{m,n}_{m_1,n_1,m_2,n_2})_r = -\frac{\mathrm{d}\sigma}{\mathrm{d}r} \frac{\psi^{m_1,n_1}\psi^{m_2,n_2}}{r^2} \frac{(F^{m,n})^2}{F^{m_1,n_1}F^{m_2,n_2}}; \tag{A.20}$$

$$\begin{aligned}
(A^{m,n}_{m_1,n_1,m_2,n_2})_\phi = {}& \frac{i}{r}\frac{\mathrm{d}\sigma}{\mathrm{d}r}\left\{ m\sigma\psi^{m_1,n_1}\psi^{m_2,n_2}\left[\frac{F^{m_2,n_2}}{F^{m_1,n_1}H^{m_2,n_2}} + \frac{F^{m_1,n_1}}{F^{m_2,n_2}H^{m_1,n_1}}\right]\right. \\
&\left. + m\psi^{m_2,n_2}\frac{\partial\psi^{m_1,n_1}}{\partial r}\frac{G^{m_1,n_1}}{F^{m_2,n_2}H^{m_1,n_1}} + m\psi^{m_1,n_1}\frac{\partial\psi^{m_2,n_2}}{\partial r}\frac{G^{m_2,n_2}}{F^{m_1,n_1}H^{m_2,n_2}}\right\} \\
&- \frac{i}{r}\frac{\partial}{\partial r}\left[\frac{\mathrm{d}\sigma}{\mathrm{d}r}\psi^{m_1,n_1}\psi^{m_2,n_2}\frac{B_{0\phi}\,F^{m,n}}{F^{m_1,n_1}F^{m_2,n_2}}\right];
\end{aligned} \tag{A.21}$$

$$\begin{aligned}
(A^{m,n}_{m_1,n_1,m_2,n_2})_\theta = {}& \frac{i}{r}\frac{\mathrm{d}\sigma}{\mathrm{d}r}\left\{ n\varepsilon\sigma\psi^{m_1,n_1}\psi^{m_2,n_2}\left[\frac{F^{m_2,n_2}}{F^{m_1,n_1}H^{m_2,n_2}} + \frac{F^{m_1,n_1}}{F^{m_2,n_2}H^{m_1,n_1}}\right]\right. \\
&\left. + n\varepsilon\psi^{m_2,n_2}\frac{\partial\psi^{m_1,n_1}}{\partial r}\frac{G^{m_1,n_1}}{F^{m_2,n_2}H^{m_1,n_1}} + n\varepsilon\psi^{m_1,n_1}\frac{\partial\psi^{m_2,n_2}}{\partial r}\frac{G^{m_2,n_2}}{F^{m_1,n_1}H^{m_2,n_2}}\right\} \\
&- i\frac{\partial}{\partial r}\left[\frac{1}{r}\frac{\mathrm{d}\sigma}{\mathrm{d}r}\psi^{m_1,n_1}\psi^{m_2,n_2}\frac{B_{0\theta}\,F^{m,n}}{F^{m_1,n_1}F^{m_2,n_2}}\right].
\end{aligned} \tag{A.22}$$

Appendix A.2. Electromagnetic torque

The electromagnetic torque along the toroidal direction, integrated on the angular co-ordinates at the generic radius r, is

$$T_{\mathrm{EM},\phi}(r) = \oiint \mathrm{d}\theta\,\mathrm{d}\phi\, r R_0^2 (\boldsymbol{j}\times\boldsymbol{b})_\phi = \oiint \mathrm{d}\theta\,\mathrm{d}\phi\, r R_0^2 (j_r b_\theta - j_\theta b_r). \tag{A.23}$$

Due to the angular integrations only the product of the perturbations gives a contribution in (A.23). Using Ampere's law (A.6), the torque is expressed by a sum over all the perturbations m, n:

$$T_{\mathrm{EM},\phi}(r) = \frac{4\pi^2 R_0^2}{\mu_0}\sum_{m,n\in\mathbb{Z}}\mathrm{Re}\left\{\frac{\partial}{\partial r}[r b_r^{m,n}(b_\phi^{m,n})^*]\right\} = -\frac{4\pi^2 R_0^2}{\mu_0}\sum_{m,n\in\mathbb{Z}}\mathrm{Im}\left\{\frac{\partial}{\partial r}[\psi^{m,n}(b_\phi^{m,n})^*]\right\}. \tag{A.24}$$

This formula is valid everywhere in the plasma, since it derives by Ampere's law only. Away from the mode resonant surfaces, we can also express the r.h.s. of (A.24) using the ideal-MHD

formulae derived in the previous section. Making use of (A.8) and (A.12) we get for the m, n contribution:

$$\text{Im}\left\{\frac{\partial}{\partial r}[\psi^{m,n}(b_\phi^{m,n})^*]\right\} = \text{Im}\left\{\frac{1}{r}\psi^{m,n}(V^{m,n})^* + \frac{\partial}{\partial r}\left[\frac{mr^2\psi^{m,n}(A_r^{m,n})^*}{H^{m,n}F^{m,n}}\right]\right\}. \tag{A.25}$$

The r.h.s of (A.25), which contains triple product of perturbations, is evaluated using the linear Newcomb's solutions, making use of (A.16), (A.19)–(A.22). We get

$$\text{Im}\left\{\frac{\partial}{\partial r}[\psi^{m,n}(b_\phi^{m,n})^*]\right\} = \sum_{\substack{m_1, n_1, m_2, n_2 \in \mathbb{Z} \\ (m_1, n_1) + (m_2, n_2) = (m, n)}} \Im_{m_1,n_1,m_2,n_2}^{m,n}. \tag{A.26}$$

For a triplet of modes such that $(m_1, n_1) + (m_2, n_2) = (m, n)$, we have defined

$$\Im_{m_1,n_1,m_2,n_2}^{m,n}(r) = \text{Im}\left\{\frac{n}{R_0}t_{m_1,n_1,m_2,n_2}^{m,n}(r) - \frac{\partial}{\partial r}\left[\frac{d\sigma}{dr}\frac{B_{0\theta}(\psi^{m_1,n_1})^*(\psi^{m_2,n_2})^*\psi^{m,n}}{F^{m_1,n_1}F^{m_2,n_2}}\right]\right\}, \tag{A.27}$$

$$\begin{aligned}
t_{m_1,n_1,m_2,n_2}^{m,n}(r) = \frac{d\sigma}{dr}&\left\{ r\psi^{m,n}(\psi^{m_1,n_1})^*\left(\frac{\partial\psi^{m_2,n_2}}{\partial r}\right)^*\frac{G^{m_2,n_2}}{F^{m,n}F^{m_1,n_1}H^{m_2,n_2}}\right. \\[2ex]
&+ r\psi^{m,n}(\psi^{m_2,n_2})^*\left(\frac{\partial\psi^{m_1,n_1}}{\partial r}\right)^*\frac{G^{m_1,n_1}}{F^{m,n}F^{m_2,n_2}H^{m_1,n_1}} \\[2ex]
&+ r\frac{\partial\psi^{m,n}}{\partial r}(\psi^{m_1,n_1})^*(\psi^{m_2,n_2})^*\frac{G^{m,n}}{F^{m_2,n_2}F^{m_1,n_1}H^{m,n}} \\[2ex]
&+ \psi^{m,n}(\psi^{m_1,n_1})^*(\psi^{m_2,n_2})^*\left[r\sigma\left(\frac{F^{m_1,n_1}}{F^{m,n}F^{m_2,n_2}H^{m_1,n_1}} + \frac{F^{m_2,n_2}}{F^{m,n}F^{m_1,n_1}H^{m_2,n_2}}\right.\right. \\[2ex]
&\left.\left.\left.+ \frac{F^{m,n}}{F^{m_2,n_2}F^{m_1,n_1}H^{m,n}}\right) + \frac{2B_{0\theta}B_{0\phi} - r\sigma(B_{0\theta}^2 + B_{0\phi}^2)}{F^{m_2,n_2}F^{m_1,n_1}F^{m,n}}\right]\right\}. \end{aligned} \tag{A.28}$$

The torque at a given radius r is therefore given by a summation over all the triplets of interacting perturbations expressed in terms of the linear Newcomb's solutions:

$$T_{\text{EM},\phi}(r) = -\frac{4\pi^2 R_0^2}{\mu_0} \sum_{\substack{m, n, m_1, n_1, m_2, n_2 \in \mathbb{Z} \\ (m_1, n_1) + (m_2, n_2) = (m, n)}} \Im_{m_1,n_1,m_2,n_2}^{m,n}. \tag{A.29}$$

It is easy to show that for such a triplet

$$\Im_{m_1,n_1,m_2,n_2}^{m,n} + \Im_{m,n,-m_2,-n_2}^{m_1,n_1} + \Im_{-m_1,-n_1,m,n}^{m_2,n_2} = 0. \tag{A.30}$$

Therefore, away from the mode resonant surfaces where ideal-MHD formulae (A.25)–(A.30) are valid, the torque (A.29) is zero: $T_{\text{EM},\phi}(r) = 0$. It is possible to show that the same results hold for the angular integrated poloidal electromagnetic torque [14]. This result is consistent with the fact that the ideal force balance relation (A.2), the starting point of this derivation, gives by definition a zero angular integrated torque. A non-zero angular integrated torque can instead develop in the vicinity of the mode resonant surfaces where ideal MHD breaks down and expression (A.29) becomes singular. In fact, according to the behaviour of the linear Newcomb's equation solution, both the derivative of $\psi^{m,n}$ and the toroidal field $b_\phi^{m,n}$, related by formula (A.8), can have a jump across the resonant surface $r_{m,n}$. Looking at formula

(A.24), the jumps in correspondence to the various resonant surfaces $r_{m,n}$ give rise to dirac-like localized torques,

$$T_{\mathrm{EM},\phi}(r) = \sum_{\substack{m \in \mathbb{Z} \\ n > 0}} \delta T_{\mathrm{EM},\phi}^{m,n} \delta(r - r_{m,n}); \qquad T_{\mathrm{EM},\theta}(r) = \sum_{\substack{m \in \mathbb{Z} \\ n > 0}} \delta T_{\mathrm{EM},\theta}^{m,n} \delta(r - r_{m,n}), \qquad \text{(A.31)}$$

where

$$\delta T_{\mathrm{EM},\phi}^{m,n} = \int_{r_{m,n}-}^{r_{m,n}+} T_{\mathrm{EM},\phi}(r) \, \mathrm{d}r = -\frac{8\pi^2 R_0^2}{\mu_0} \mathrm{Im}[\psi^{m,n}(b_\phi^{m,n})^*]_{r_{m,n}-}^{r_{m,n}+} \qquad m \in \mathbb{Z}, n > 0. \quad \text{(A.32)}$$

Moreover, as shown in [1], between the poloidal and toroidal components of the torque a simple proportional relation holds:

$$\delta T_{\mathrm{EM},\theta}^{m,n} = -\frac{m}{n} \delta T_{\mathrm{EM},\phi}^{m,n}. \tag{A.33}$$

The summation in (A.31) runs over the resonant surfaces, so only the positive n are considered; the contributions of both the complex conjugate harmonics (m, n), $(-m, -n)$ for a given resonant surface are included in the factor 8 in front of the r.h.s of (A.32). The important point is that the discontinuities associated with the localized torques in (A.32) can be obtained from the ideal-MHD expressions (A.26)–(A.28). We start observing that, despite the presence of singularities at the mode resonant surfaces, expression (A.28) is integrable taking the Cauchy principal value: in fact, *assuming that the three modes involved have different resonant surfaces*, according to expansion (A.18) these singularities are of the types $1/x$ and $\ln|x|$. Therefore, we can perform a symbolic integration of (A.26): we have to separate the region $0 < r < r_{m,n}$, where the expression consistent with the condition $\psi^{m,n}(0) = 0$ holds:

$$\mathrm{Im}[\psi^{m,n}(b_\phi^{m,n})^*] = \sum_{\substack{m_1, n_1, m_2, n_2 \in \mathbb{Z} \\ (m_1, n_1) + (m_2, n_2) = (m, n)}} \mathrm{Im}\left\{ \frac{n}{R_0} P \int_0^r t_{m_1,n_1,m_2,n_2}^{m,n}(\xi) \, \mathrm{d}\xi \right.$$

$$\left. - \left[\frac{\mathrm{d}\sigma}{\mathrm{d}r} \frac{B_{0\theta}(\psi^{m_1,n_1})^*(\psi^{m_2,n_2})^* \psi^{m,n}}{F^{m_1,n_1} F^{m_2,n_2}} \right] \right\}, \tag{A.34}$$

from the region $r_{m,n} < r$ where another expression consistent with the edge value at a given radius $a \leqslant \bar{r} \leqslant r_{\mathrm{wi}}$ in the vacuum region ($\sigma = 0$) between the plasma and the shell holds:

$$\mathrm{Im}[\psi^{m,n}(b_\phi^{m,n})^*] = \sum_{\substack{m_1, n_1, m_2, n_2 \in \mathbb{Z} \\ (m_1, n_1) + (m_2, n_2) = (m, n)}} \mathrm{Im}\left\{ \frac{n}{R_0} P \int_{\bar{r}}^r t_{m_1,n_1,m_2,n_2}^{m,n}(\xi) \, \mathrm{d}\xi \right.$$

$$\left. - \left[\frac{\mathrm{d}\sigma}{\mathrm{d}r} \frac{B_{0\theta}(\psi^{m_1,n_1})^*(\psi^{m_2,n_2})^* \psi^{m,n}}{F^{m_1,n_1} F^{m_2,n_2}} \right] \right\} + \mathrm{Im}[\psi^{m,n}(b_\phi^{m,n})^*]_{\bar{r}}. \tag{A.35}$$

These two regions are separated by the resonant surface $r = r_{m,n}$, since at that point the quantity $\mathrm{Im}[\psi^{m,n}(b_\phi^{m,n})^*]$ can have a jump. This jump, and therefore the localized torque, is given by the difference in (A.34) and (A.35) evaluated at $r = r_{m,n}$:

$$\delta T_{\mathrm{EM},\phi}^{m,n} = \frac{8\pi^2 R_0 n}{\mu_0} \left\{ \sum_{\substack{m_1, n_1, m_2, n_2 \in \mathbb{Z} \\ (m_1, n_1) + (m_2, n_2) = (m, n)}} \mathrm{Im}\left[P \int_0^a t_{m_1,n_1,m_2,n_2}^{m,n}(r) \, \mathrm{d}r \right] \right.$$

$$\left. + \mathrm{Im}\left[f^{m,n} \frac{\partial \psi^{m,n}}{\partial r} (\psi^{m,n})^* \right]_{\bar{r}} \right\}. \tag{A.36}$$

In this expression the first term represents the electromagnetic torque developed by the non-linear interaction between the modes expressed in terms of the linear Newcomb's solutions;

here the integral can be limited between $[0, a]$, since the integrand is zero in vacuum. The second term is the edge contribution present in (A.35), expressed using (A.8) taking into account that $A = 0$ in vacuum: it represents the electromagnetic torque produced by the interaction between the m, n radial field and the m, n eddy currents into the shell. This term was not present in the analogous formulae of [14], since it was supposed that an ideal shell surrounded the plasma, in which case $\psi^{m,n}(\bar{r} = r_{\text{wi}}) = 0$. We also express this contribution using the linear Newcomb's solutions. For both terms of (A.36) it is convenient to introduce the solution basis functions defined with formula (2), taking into account that $\psi^{m,n}(r, t) = \Psi_{\text{s}}^{m,n}(t)\hat{\psi}_{\text{s}}^{m,n}(r) + \Psi_{\text{wi}}^{m,n}(t)\hat{\psi}_{\text{wi}}^{m,n}(r)$ in the region $0 < r \leqslant r_{\text{wi}}$ considered here. Concerning the edge contribution, since for the linear solutions equation (A.17) implies that

$$\text{Im}\left\{\frac{\partial}{\partial r}\left[f^{m,n}\frac{\partial \psi^{m,n}}{\partial r}(\psi^{m,n})^*\right]\right\} = 0,$$

taking into account the vanishing conditions for $\psi^{m,n}$ in the origin and definition (3), we have

$$\text{Im}\left[f^{m,n}\frac{\partial \psi^{m,n}}{\partial r}(\psi^{m,n})^*\right]_{\bar{r}} = \text{Im}\left[f^{m,n}\frac{\partial \psi^{m,n}}{\partial r}(\psi^{m,n})^*\right]_{r_{m,n}-}^{r_{m,n}+} = \frac{E_{\text{ws}}^{m,n}}{H^{m,n}(r_{m,n})}\text{Im}[\Psi_{\text{wi}}^{m,n}(\Psi_{\text{s}}^{m,n})^*].$$

(A.37)

We finally get

$$\delta T_{\text{EM},\phi}^{m,n} = \frac{8\pi^2 R_0 n}{\mu_0} \sum_{\substack{m_1, n_1, m_2, n_2 \in \mathbb{Z} \\ (m_1, n_1) + (m_2, n_2) = (m, n)}} \sum_{i, j, k \in \{\text{s,wi}\}} \text{Im}[\Psi_i^{m,n}(\Psi_j^{m_1,n_1})^*(\Psi_k^{m_2,n_2})^*]$$

$$\cdot \Gamma_{m_1,n_1,m_2,n_2}^{m,n}(i, j, k) + \frac{8\pi^2 R_0 n}{\mu_0}\frac{E_{\text{ws}}^{m,n}}{H^{m,n}(r_{m,n})}\text{Im}[\Psi_{\text{wi}}^{m,n}(\Psi_{\text{s}}^{m,n})^*],$$

(A.38)

where we have defined the real quantities

$$\Gamma_{m_1,n_1,m_2,n_2}^{m,n}(i, j, k) = P\int_0^a \hat{t}_{m_1,n_1,m_2,n_2}^{m,n}(i, j, k, r)\,\mathrm{d}r \qquad i, j, k \in \{\text{s, wi}\}$$

(A.39)

being

$$\hat{t}_{m_1,n_1,m_2,n_2}^{m,n}(i, j, k, r) = \frac{\mathrm{d}\sigma}{\mathrm{d}r}\left\{r\hat{\psi}_i^{m,n}\hat{\psi}_j^{m_1,n_1}\frac{\mathrm{d}\hat{\psi}_k^{m_2,n_2}}{\mathrm{d}r}\frac{G^{m_2,n_2}}{F^{m,n}F^{m_1,n_1}H^{m_2,n_2}}\right.$$

$$+ r\hat{\psi}_i^{m,n}\frac{\mathrm{d}\hat{\psi}_j^{m_1,n_1}}{\mathrm{d}r}\hat{\psi}_k^{m_2,n_2}\frac{G^{m_1,n_1}}{F^{m,n}F^{m_2,n_2}H^{m_1,n_1}}$$

$$+ r\frac{\mathrm{d}\hat{\psi}_i^{m,n}}{\mathrm{d}r}\hat{\psi}_j^{m_1,n_1}\hat{\psi}_k^{m_2,n_2}\frac{G^{m,n}}{F^{m_2,n_2}F^{m_1,n_1}H^{m,n}}$$

$$+ \hat{\psi}_i^{m,n}\hat{\psi}_j^{m_1,n_1}\hat{\psi}_k^{m_2,n_2}\left[r\sigma\left(\frac{F^{m_1,n_1}}{F^{m,n}F^{m_2,n_2}H^{m_1,n_1}} + \frac{F^{m_2,n_2}}{F^{m,n}F^{m_1,n_1}H^{m_2,n_2}}\right.\right.$$

$$\left.\left.+ \frac{F^{m,n}}{F^{m_2,n_2}F^{m_1,n_1}H^{m,n}}\right) + \frac{2B_{0\theta}B_{0\phi} - r\sigma(B_{0\theta}^2 + B_{0\phi}^2)}{F^{m_2,n_2}F^{m_1,n_1}F^{m,n}}\right]\right\};$$

$i, j, k \in \{\text{s, wi}\}.$ (A.40)

Formulae (A.33) and (A.38) express the electromagnetic torque which develops at the resonant surface m, n in terms of the amplitudes and phases at the resonant surfaces and at the inner shell radius of the m, n mode and of all the modes involved in the non-linear interaction with the m, n

mode. All the real coefficients present in (A.38) are obtained from the solutions $\hat{\psi}_s(r)$, $\hat{\psi}_{wi}(r)$ of the linear Newcomb's equation for all the modes involved. Formulae (A.33) and (A.38) generalize to the resistive shell boundary condition the result of [14]. This condition, besides the edge contribution, introduces eight coefficients (A.39) for a given triplet of modes, while in the ideal shell case ($\Psi_{wi} = 0$) we would have just the single coefficient $\Gamma_{m_1,n_1,m_2,n_2}^{m,n}(s, s, s)$.

Appendix B. Coils voltages

The relationship between the coils currents and voltages is

$$V_{i,j} = \frac{R_c}{N_c} I_{i,j} + c R_0 \Delta\theta \Delta\phi N_c \frac{d}{dt} b_{i,j}^r(c), \tag{B.1}$$

where $b_{i,j}^r(c)$ is the average radial field enclosed by the i, j coil. Taking the m, n discrete Fourier harmonic of (B.1) we have

$$V_c^{m,n} = \frac{R_c}{N_c} I_c^{m,n} + c R_0 \Delta\theta \Delta\phi N_c \frac{d}{dt} \sum_{\substack{l, k \in Z \\ p = m + lM \\ q = n + kN}} b_r^{p,q}(c) f(p, q) \tag{B.2}$$

being

$$f(p, q) = \frac{\sin\left(q\frac{\Delta\phi}{2}\right)}{q\frac{\Delta\phi}{2}} \frac{\sin\left(p\frac{\Delta\theta}{2}\right)}{p\frac{\Delta\theta}{2}}.$$

The second term of (B.2) is the time variation of the radial flux enclosed by the coils determined by the m, n mode and by the sidebands ($l \neq 0$ or $k \neq 0$) produced by the coils. By combining (4) and (27), for the m, n mode we have $b_r^{m,n}(c) = i\Psi_c^{m,n}/c = i(L^{m,n}I_c^{m,n} - \Psi_{we}^{m,n}E_{wc}^{m,n})/(cE_c^{m,n})$. As shown in [8], the sidebands can be safely computed from the coils current using the vacuum approximation. Here we adopt the further simplification of neglecting the shell contribution (justified by the fact that we are considering the sideband at $r = c$), in which case there is a simple proportional relation between the p, q sideband and the current discrete harmonic $I_c^{m,n}$:

$$b_r^{p,q}(c) = -\mu_0 K_p'\left(\frac{|q|c}{R_0}\right) I_p'\left(\frac{|q|c}{R_0}\right) \frac{q^2 c}{R_0^2} f(p, q) I_c^{m,n}. \tag{B.3}$$

Therefore we arrive at the final expression:

$$V_c^{m,n} = \frac{R_c}{N_c} I_c^{m,n} + l^{m,n} \frac{d}{dt} I_c^{m,n} - \frac{4R_0 N_c}{mn} \sin\left(n\frac{\Delta\phi}{2}\right) \sin\left(m\frac{\Delta\theta}{2}\right) \frac{i E_{wc}^{m,n}}{E_c^{m,n}} \frac{d}{dt} \Psi_{we}^{m,n}, \tag{B.4}$$

$$l^{m,n} = -\mu_0 N_c \Delta\theta \Delta\phi \left[\frac{c^2}{R_0} \sum_{\substack{(l, k) \in Z^2 - (0, 0) \\ p = m + lM \\ q = n + kN}} K_p'\left(\frac{|q|c}{R_0}\right) I_p'\left(\frac{|q|c}{R_0}\right) q^2 f(p, q)^2 \right.$$

$$\left. + H^{m,n}(c) \frac{R_0}{E_c^{m,n}} f(m, n)^2 \right]. \tag{B.5}$$

References

[1]　Fitzpatrick R 1993 *Nucl. Fusion* **33** 1049
[2]　Fitzpatrick R *et al* 1999 *Phys. Plasmas* **6** 3878
[3]　Sonato P *et al* 2003 *Fusion Eng. Des.* **66–68** 161
[4]　Bishop C M 1989 *Plasma Phys. Control. Fusion* **31** 1179
[5]　Alper B *et al* 1989 *Plasma Phys. Control. Fusion* **31** 205
[6]　Gimblett C G and Watkins M L *Proc. 7th European Conf. on Controlled Fusion and Plasma Physics (Lausanne)*
　　　vol 1 (Geneva: European Physical Society) p103
[7]　Rusbridge M G 1991 *Plasma Phys. Control. Fusion* **33** 1381
[8]　Zanca P *et al* 2007 *Nucl. Fusion* **47** 1425
[9]　Marrelli L *et al* 2007 *Plasma Phys. Control. Fusion* **49** B359
[10]　Guo S C and Chu M S 2004 *Phys. Plasmas* **11** 4050
[11]　Gimblett C G 1986 *Nucl. Fusion* **26** 617
[12]　Fitzpatrick R and Zanca P 2002 *Phys. of Plasmas* **9** 2707
[13]　Arcis N, Escande D F and Ottaviani M 2007 *Phys. Plasmas* **14** 032308
[14]　Fitzpatrick R 1999 *Phys. Plasmas* **6** 1168
[15]　Newcomb W A 1960 *Ann. Phys. (N.Y.)* **10** 232
[16]　Zanca P and Terranova D 2004 *Plasma Phys. Control. Fusion* **46** 1115
[17]　Fitzpatrick R and Yu E P 1999 *Phys. Plasmas* **6** 3536
[18]　Marchiori G *et al* 2008 Advances in MHD-control in RFX-mod *35th EPS Conf. (Hersonissos, Crete, Greece)*
[19]　Almagri A F *et al* 1998 *Phys. Plasmas* **5** 3982
[20]　Carraro L 1998 *et al Plasma Phys. Control. Fusion* **40** 1021
[21]　Navratil G A *et al* 1998 *Phys. Plasmas* **5** 1855
[22]　Lorenzini R *et al* 2008 *Phys. Rev. Lett.* **101** 025005
[23]　Marquez H J 2003 *Nonlinear Control Systems, Analysis and Design* (New York: Wiley-Interscience)
[24]　Antoni V *et al* 1986 *Nucl. Fusion* **26** 1711